

GLOBAL AND SEASONAL EFFECTS OF
LIGHTNING-INDUCED ELECTRON PRECIPITATION

A DISSERTATION
SUBMITTED TO THE COMMITTEE ON GRADUATE STUDIES
OF STANFORD UNIVERSITY
IN PARTIAL FULFILLMENT OF THE REQUIREMENTS
FOR THE DEGREE OF
DOCTOR OF PHILOSOPHY
IN
ELECTRICAL ENGINEERING

Austin Patrick Sousa

January 2018

© Copyright by Austin Patrick Sousa 2018
All Rights Reserved

I certify that I have read this dissertation and that, in my opinion, it is fully adequate in scope and quality as a dissertation for the degree of Doctor of Philosophy.

(Prof. Sigrid Close) Principal Adviser

I certify that I have read this dissertation and that, in my opinion, it is fully adequate in scope and quality as a dissertation for the degree of Doctor of Philosophy.

(Prof. Robert Marshall, University of Colorado Boulder)

I certify that I have read this dissertation and that, in my opinion, it is fully adequate in scope and quality as a dissertation for the degree of Doctor of Philosophy.

(Prof. Antony Fraser-Smith)

Approved for the Stanford University Committee on Graduate Studies

Preface

This thesis tells you all you need to know about...

Acknowledgments

(Acknowledgements go here)

Contents

Preface	iv
Acknowledgments	v
1 Introduction	1
1.1 The Space Environment	1
1.2 Motivation	1
1.3 Previous Work	1
1.4 Thesis Organization	1
2 Physics and Methods	2
2.1 Overview of Plasma Physics	2
2.1.1 Single Particle Motion	3
2.1.2 The Loss Cone	6
2.1.3 Waves in Plasmas	8
2.2 Ray Tracing and Landau Damping	14
2.2.1 Ray Tracing	14
2.2.2 Landau Damping	16
2.3 Lightning Illumination Model	18
2.4 Trans-Ionosphere Attenuation	20
2.5 Wave-Particle Interactions	23
2.5.1 Resonant Interactions	24
2.5.2 Recovering Wave Amplitudes from Poynting Flux	27
2.6 Environment Models	28

2.6.1	Magnetic Field	28
2.6.2	Plasmasphere	30
2.6.3	Ionosphere	34
2.6.4	The Radiation Belts	34
3	VLF energy in the Near-Earth Environment	38
3.1	Methodology	38
3.2	Persistent Energy from a Single Flash	47
3.2.1	Radiated power above the ionosphere	47
3.2.2	Gridding and Interpolation	47
3.3	Global Energy Density	47
4	3D Modeling of LEP	48
4.1	Overview of Previous Work	48
5	Global and Seasonal Estimates of LEP	49
5.1	Overview of Previous Work	49
6	Satellite Instrumentation for LEP Measurement	50
6.1	VPM Mission Overview	50
6.2	Hardware Architecture	50
6.2.1	Wave Measurement	50
6.2.2	Particle Measurement	50
6.3	Firmware Architecture	50
7	Conclusions	51
A	Reference Equations	52
A.1	Landau Damping	52
B	Runge-Kutta Methods	55
	Bibliography	56

List of Tables

3.1	Simulation Parameters	40
-----	---------------------------------	----

List of Figures

2.1	An example of a “magnetic bottle” particle trap	5
2.2	Adiabatic motion in the Earth’s magnetic field	7
2.3	Loss cone illustration	8
2.4	An ω -K diagram for the cold, four-component dispersion relation, for parallel propagation at $L \approx 3$	13
2.5	Example ray tracing	16
2.6	Phase-space density functions	19
2.7	Time and frequency profiles of the lightning illumination model . . .	21
2.8	Trans-Ionosphere attenuation curves for day and night	24
2.9	Illustration of resonant wave-particle interactions	25
2.10	Magnetic field models	31
2.11	L-shell contours on the Earth’s surface	32
2.12	A Comparison of three plasmasphere electron density models	33
2.13	Ionosphere density profile	35
2.14	AE8 integral flux model	36
2.15	Pitch-angle distribution functions	37
3.1	Energy density calculation block diagram	39
3.2	Illumination pattern below the ionosphere	40
3.3	Illumination pattern above the ionosphere	41
3.4	Energy above the ionosphere due to a single flash	42

3.5	An illustration of the interpolation scheme. (a) Energy at the top of the ionosphere is divided into cells, in latitude, longitude, and frequency. Shown here with 5° cells (much larger than used in simulation). The plotted energy is integrated over frequency. (b) Illustration of the guide ray method. Input energy is integrated between a set of guide rays, spaced in latitude, longitude, and frequency. This energy is then averaged over a 4-dimensional volume, bounded by two adjacent timesteps $t - 1, t$ of the guide rays.	43
3.6	Illustration of the Delaunay interpolation method, shown here in three dimensions (e.g., for a single frequency).	44
3.7	Fine-scale frequency interpolation.	45
3.8	Illustration of a convex hull in two dimensions.	46
3.9	Block diagram	46
3.10	Block diagram	46
3.11	Block diagram	47
3.12	Average energy density vs L and frequency	47

Chapter 1

Introduction

1.1 The Space Environment

1.2 Motivation

1.3 Previous Work

1.4 Thesis Organization

Chapter 2

Background Physics and Description of Methods

2.1 Overview of Plasma Physics

A *plasma* is a quasi-neutral gas of ions, electrons, and neutral particles, which exhibit collective behavior. Plasmas can behave in similar ways to a conventional fluid – they can flow, they can be compressible, they can be turbulent, and so on – however the addition of charged particles facilitates many behaviors unique to a plasma. Charged particles can interact with each other not just through ballistic collisions, but at a distance through electromagnetic forces. The bulk motion of a plasma can be manipulated through electric and magnetic fields; conversely a plasma can have a substantial effect on the propagation of radio waves passing through it.

A plasma can be analyzed in several different domains: Single particle motion; fluid approximations; and full kinematic solutions. In this work we treat the motions of electrons in the single particle domain, which is a natural choice for the sparse densities and small gyroradii of radiation belt electrons. To understand the behavior of radio waves propagating through a plasma, we treat the background as a smooth dielectric medium.

2.1.1 Single Particle Motion

The high energies and sparse densities of the radiation belts lend themselves very well to a single-particle approximation. Many of the basic behaviors and quantities in plasma physics can be understood through studying the motion of a single particle.

The fundamental equation of motion for a charged particle in an electromagnetic field is given by the Lorentz force:

$$\mathbf{F} = \frac{d\mathbf{p}}{dt} = q(\mathbf{E} + \mathbf{v} \times \mathbf{B}) \quad (2.1)$$

Where q represents the particle's charge, \mathbf{E} and \mathbf{B} represent the electric and magnetic fields, and \mathbf{v} the particle's velocity, shown here in a non-relativistic frame.

Electric fields simply apply a force in the direction of the field. However, note that a cross product is perpendicular to both terms – therefore any forces induced by the magnetic field will be perpendicular to the particle's velocity. The magnetic field is a *conservative* force, in that a stationary magnetic field cannot directly impart energy into a particle, but can alter a particle's trajectory. The particle will therefore have a net drift in the direction of the electric field, while exhibiting a helical motion around the magnetic field.

We can then split the velocity vector into two quantities – v_{\parallel} parallel to the magnetic field, and v_{\perp} perpendicular to the magnetic field. Two characteristic values arise from this motion: the radius of the particle's rotation around the magnetic field, known as the *gyroradius* or the *Larmor radius*:

$$r_l = \frac{mv_{\perp}}{qB} \quad [\text{m}] \quad (2.2)$$

and the rotation frequency, known as the *gyrofrequency* or *cyclotron frequency*:

$$\omega_c = \frac{v_{\perp}}{r_l} = \frac{qB}{m} \quad [\text{rad/sec}] \quad (2.3)$$

By integrating the particle's momentum over a single gyrorotation, we arrive at a third fundamental quantity known as the magnetic moment, or the *first adiabatic*

invariant:

$$\mu = \frac{mv_{\perp}^2}{2B} \quad (2.4)$$

In situations where the magnetic field varies slowly (e.g., on spatial scales much greater than the gyroradius), μ remains a constant of motion.

A final parameter to describe a particle's motion is its *pitch angle*, the angle between the velocities perpendicular and parallel to the magnetic field:

$$\alpha = \tan^{-1} \left(\frac{v_{\perp}}{v_{\parallel}} \right) \quad (2.5)$$

The first adiabatic invariant describes an implicit relationship between the magnetic field strength and a particle's pitch angle at a given point. Combining the first adiabatic invariant with conservation of kinetic energy, we can deduce an expression for magnetic trapping – that is, the magnetic field strength in which a particle exhibiting helical motion along a magnetic field line will turn around.

$$E = \frac{1}{2}mv^2 \quad (2.6)$$

$$= \frac{1}{2}m(v_{\parallel}^2 + v_{\perp}^2) \quad (2.7)$$

$$= \frac{1}{2}mv^2(\cos^2\alpha + \sin^2\alpha) \quad (2.8)$$

At a reflection point, the particle's kinetic energy will be entirely in the perpendicular mode:

$$\frac{v_{\perp 0}^2}{B_0} = \frac{v_{\perp 1}^2}{B_1} \quad (2.9)$$

$$\frac{v^2 \sin^2(\alpha)}{B_0} = \frac{v^2}{B_1} \quad (2.10)$$

$$\sin^2(\alpha) = \frac{B_0}{B_1} \quad (2.11)$$

A charged particle in a magnetic field will therefore be constrained to rotate around a field line, and feel an opposing longitudinal force as the field intensity increases.

If the magnetic field is such that there are two regions of increasing intensity, separated by a reasonable distance, the particle may bounce back and forth, reflecting at turning points given by equation 2.11. Such a field configuration is known as a “magnetic bottle” particle trap, as shown in figure 2.1. A key observation is that the reflection point is independent of energy, and depends only on the ratio of magnetic field strengths and the particle’s initial pitch angle.

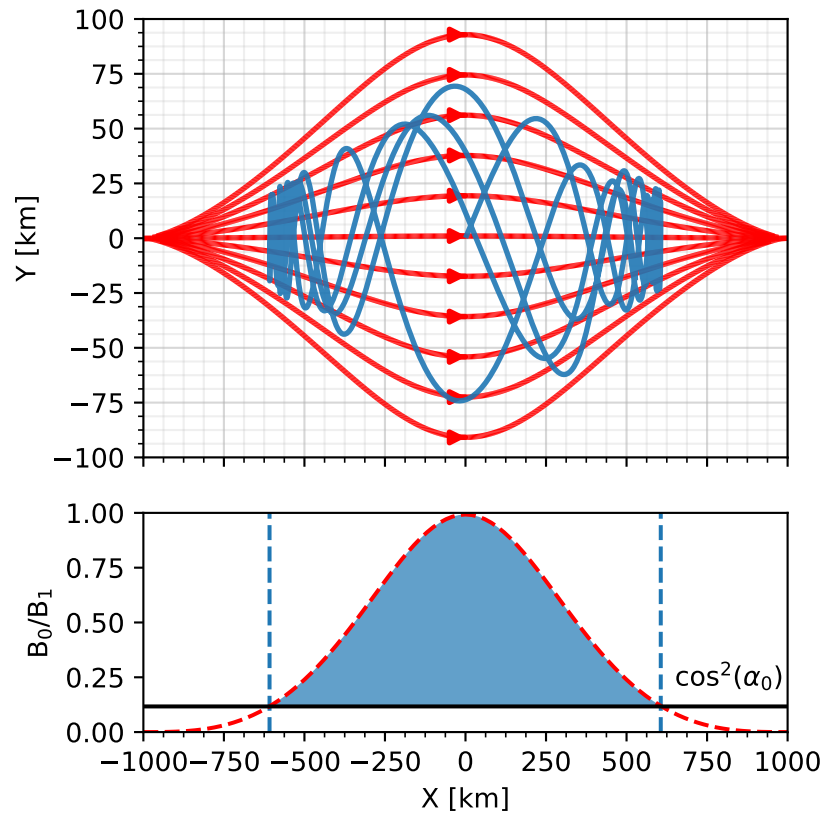


Figure 2.1: An example of a “magnetic bottle” particle trap. The top plot shows the trajectory of an electron with an initial pitch angle $\alpha_0 = 20^\circ$. The bottom plot shows the magnetic field ratio B_0/B_1 , with the particle’s reflection points shown as vertical lines.

2.1.2 The Loss Cone

A magnetic bottle trap need not be linearly-arranged, as it is in figure 2.1; we require only that the magnetic field be slowly-varying with respect to the particle's gyroradius. The Earth's dipole magnetic field forms a natural and effective particle trap, which dominates the morphology of charged particle populations surrounding the Earth. The motion of a charged particle in the Earth's magnetic field can be broken into three components (see figure 2.2):

- a rapid gyrorotation around the background magnetic field
- a “bouncing” motion between the north and south poles, with periods ranging from milliseconds to several seconds; and
- a slower, longitudinal drift, causing the particles to precess around the earth on the order of minutes to days, resulting from the magnetic field gradient

We can average the particle's motion over a single gyrorotation to define a *guiding center*, the trajectory of which follows the background magnetic field line.

As described previously, a trapped particle's reflection points are defined by the particle's initial pitch angle, and the strength of the magnetic field. In the case of the Earth, however, these turning points are limited in feasibility as well – for instance, a particle naturally cannot have a reflection point lower than the Earth's surface. Moreover, the Earth's neutral atmosphere becomes exponentially more-dense with decreasing altitude; particles reflecting at an altitude below ≈ 100 km will encounter a significant neutral molecule population, and stand a very good chance of colliding. A collision with atmospheric constituents can result in the particle losing some, or all, of its kinetic energy through ionization, and may be completely lost from the system, or return onto a different fieldline, with a different energy and/or pitch angle (Cotts, 2011).

With an understanding of the dense neutral atmosphere, we can define a critical altitude – 100 km here and in previous work – and thus a critical pitch angle, known

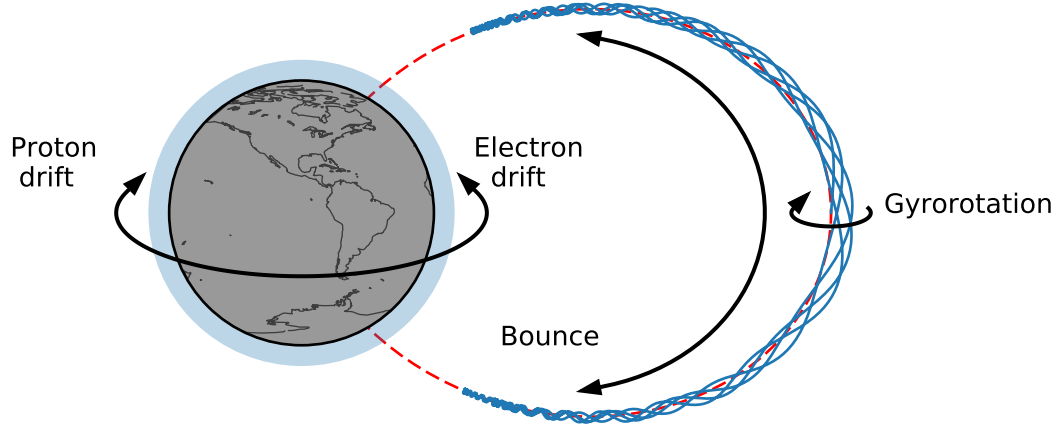


Figure 2.2: Illustration of the various motions exhibited by a charged particle in the Earth's magnetic field

as the (bounce) *loss-cone angle*:

$$\sin \alpha_{lc} = \sqrt{\frac{B(\mathbf{r})}{B_{h_m}}} \quad (2.12)$$

where h_m is the reflection height, and $B(\mathbf{r})$ is measured at the reference point – either the particle's current location for a *local loss cone angle*, or at the equator along the field line for the *equatorial loss cone angle*.

In the case of a dipole magnetic field model, we can determine the equatorial loss cone explicitly:

$$\sin \alpha_{lc} = \sqrt{\frac{\zeta_m^3}{\sqrt{1 + 3(1 - \zeta_m)}}} \quad \zeta_m = (R_e + h_m)/(LR_e) \quad (2.13)$$

where $R_e = 6371$ km is the radius of the Earth, and L is the *L-shell* of interest (see

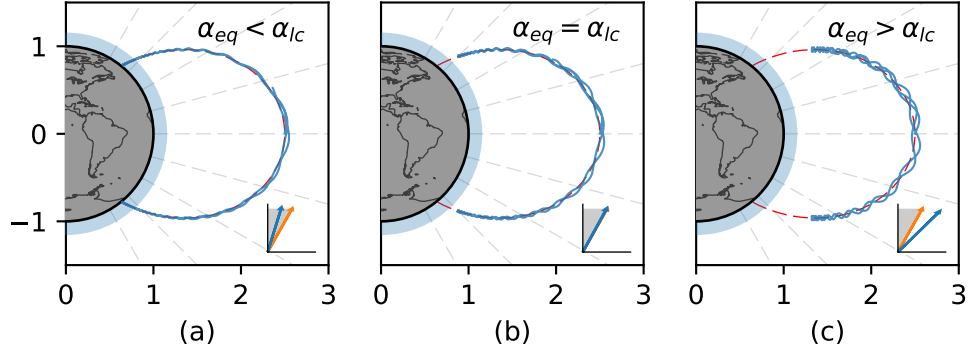


Figure 2.3: An illustration of the loss cone. The trajectory of a test electron is shown in blue, for three different equatorial pitch angles: (a) a precipitating particle with a pitch angle within the loss cone, (b) at the edge of the loss cone, and (c), a stably-trapped particle with a pitch angle well outside the loss cone.

section 2.6.1).

Bounce and Drift Loss Cones We have discussed what is known as the *bounce loss cone*. Also of interest in the study of the space environment is the *drift loss cone*. The drift loss cone is the largest loss cone along the same L-shell, as it varies longitudinally. Conceptually, as a particle drifts longitudinally, it may encounter a different loss cone, and could precipitate at certain longitudes, but not others. At some point along this longitudinal precession, the particle will encounter the maximum bounce loss cone, and precipitate (see *Cotts (2011)*, figure 2.3).

Under a simple dipole magnetic field model, the bounce loss cone is uniform around the globe, and the bounce and drift loss cones are identical. Within this dissertation, we primarily work with a dipole magnetic field model, and consider only the bounce loss cone.

2.1.3 Waves in Plasmas

Previously, we have described the motion of a charged particle under the influence of an electromagnetic field. the single-particle approximation provides enormous insight

into the dynamics of a sparsely-populated plasma. Next, we must consider the inverse system: how the charged particles in a plasma dictate the characteristic behaviors of an electromagnetic wave propagating through it.

An electromagnetic wave can accelerate a charged particle; conversely, an accelerating or decelerating particle induces its own electromagnetic field. It would seem, then, that the behavior of an electromagnetic field in a plasma is simply the summation of the contributions of each particle and some incident wave source. However, the complexity of this brute-force approach quickly becomes intractable for even a handful of particles. The universal approach taken then is to abstract the complicated interplay of waves and particles into a wave moving through a dielectric medium, described only by the various constituent densities, temperatures, and background fields within a given volume.

As with any electromagnetic problem, we begin with Maxwell's equations, shown here in their non-relativistic, differential form, in SI units:

$$\nabla \cdot \mathbf{E} = \frac{\rho}{\epsilon_0} \quad (2.14)$$

$$\nabla \cdot \mathbf{B} = 0 \quad (2.15)$$

$$\nabla \times \mathbf{E} = -\frac{\partial \mathbf{B}}{\partial t} \quad (2.16)$$

$$\nabla \times \mathbf{B} = \mu_0 \mathbf{J} + \frac{1}{c^2} \frac{\partial \mathbf{E}}{\partial t} \quad (2.17)$$

\mathbf{E} and \mathbf{B} denote the electric and magnetic fields; μ_0 and ϵ_0 denote the magnetic permeability and electric permittivity of free space; and $c = \sqrt{\frac{1}{\mu_0 \epsilon_0}}$ is the speed of light in vacuum. The terms ρ and \mathbf{J} represent the local charge density and current density, both of which may be functions of position and time.

By taking the curl of equation 2.16 and substituting in the time derivative of equation 2.17, and making use of the vector identity $\nabla \times \nabla \times \mathbf{E} = \nabla(\nabla \cdot \mathbf{E}) - \nabla^2 \mathbf{E}$, we have:

$$\nabla^2 \mathbf{E} - \frac{\nabla \rho}{\epsilon_0} = \mu_0 \frac{\partial \mathbf{J}}{\partial t} + \frac{1}{c^2} \frac{\partial^2 \mathbf{E}}{\partial t^2} \quad (2.18)$$

In the absence of charges or currents ($\rho = 0$, $\partial \mathbf{J} / \partial t = 0$), the equation reduces to the free-space wave equation:

$$\nabla^2 \mathbf{E} = \frac{1}{c^2} \frac{\partial^2 \mathbf{E}}{\partial t^2} \quad (2.19)$$

Next, we search for harmonic perturbations of the form:

$$\mathbf{E}(\mathbf{r}, t) = \mathbf{E}_1 e^{i(\omega t - \mathbf{k} \cdot \mathbf{r})} \quad (2.20)$$

$$\mathbf{B}(\mathbf{r}, t) = \mathbf{B}_0 + \mathbf{B}_1 e^{i(\omega t - \mathbf{k} \cdot \mathbf{r})} \quad (2.21)$$

$$\mathbf{J}(\mathbf{r}, t) = \mathbf{J}_1 e^{i(\omega t - \mathbf{k} \cdot \mathbf{r})} \quad (2.22)$$

where ω is the wave angular frequency, \mathbf{k} is the wave vector, or spatial frequency, and \mathbf{r} is the spatial coordinate. Two fundamental parameters of an electromagnetic wave are the *phase velocity*, ω/k , and the *group velocity*, $\partial \omega / \partial k$. The relation between the temporal and spatial frequencies is known as the *dispersion relation*.

From here we follow the derivation and convention used by *Stix* (1992) and *Bitencourt* (2004). In general, a plasma is comprised of several different species of constituent particles – positively and negatively charged particles necessary to maintain a quasi-neutral plasma. While the dispersion relations of different species cannot be simply added, their effects can be summed to form the displacement current \mathbf{J} :

$$\mathbf{J} = \sum_s \mathbf{J}_s = \sum_s n_s q_s \mathbf{u}_s \quad (2.23)$$

where n , q , and \mathbf{u} represent the (number) density, charge, and velocity of a particular species s .

We make the assumption that the plasma is *cold* – that is, that all particles of a particular species are moving with the same velocity \mathbf{u}_s , with no thermal variation. Were we to relax this assumption, each species density would have a distribution function in both position and momentum, $n = n(\mathbf{r}, \mathbf{p})$; the total current would then be an integration over momentum for each species. For a treatment of a hot plasma, see the work by *Sazhin* (1993).

Next, we note that, in a cold plasma assumption, the Lorentz force (equation 2.1)

can be written for each species:

$$m_s \frac{d\mathbf{u}_s}{dt} = q_s (\mathbf{E} + \mathbf{u}_s \times \mathbf{B}) \quad (2.24)$$

Combining equations 2.20 – 2.22, 2.23, and 2.24, and assuming a coordinate system with the background magnetic field \mathbf{B}_0 aligned with the z-axis, we arrive at an expression for the *cold-plasma dielectric tensor*:

$$\boldsymbol{\epsilon} \cdot \mathbf{E} = \begin{pmatrix} S & -iD & 0 \\ iD & S & 0 \\ 0 & 0 & P \end{pmatrix} \begin{pmatrix} E_x \\ E_y \\ E_z \end{pmatrix} \quad (2.25)$$

The various summations over each constituent species are incorporated into the so-called Stix parameters (*Stix* (1992)):

$$S = \frac{1}{2}(R + L) \quad D = \frac{1}{2}(R - L) \quad (2.26)$$

$$R = 1 - \sum_s \frac{\omega_{ps}^2}{\omega(\omega + \omega_{cs})}; \quad L = 1 - \sum_s \frac{\omega_{ps}^2}{\omega(\omega - \omega_{cs})}; \quad P = 1 - \sum_s \frac{\omega_{ps}^2}{\omega^2} \quad (2.27)$$

where $\omega_{ps} = n_s q_s^2 / \epsilon_0 m_s$ and $\omega_{cs} = q_s B_0 / m_s$ are the plasma and cyclotron frequencies for species s .

Dispersion Relation

With the dielectric tensor now determined, we can derive the relationship between ω and \mathbf{k} , known as the dispersion relation. Equation 2.18 can be written as:

$$\boldsymbol{\eta} \times \boldsymbol{\eta} \times \mathbf{E} + \boldsymbol{\epsilon} \cdot \mathbf{E} = 0 \quad (2.28)$$

where $\eta = kc/\omega$ is the wave refractive index. Assuming a wave propagating with some angle θ between η and the background magnetic field, we arrive at:

$$\begin{pmatrix} S - \eta^2 \cos^2 \theta & -iD & \eta^2 \cos \theta \sin \theta \\ iD & S - \eta^2 & 0 \\ \eta^2 \cos \theta \sin \theta & 0 & P - \eta^2 \sin^2 \theta \end{pmatrix} \begin{pmatrix} E_x \\ E_y \\ E_z \end{pmatrix} = 0 \quad (2.29)$$

Taking the determinant of 2.29 yields the *cold-plasma dispersion relation*:

$$A\eta^4 - B\eta^2 + C = 0 \quad (2.30)$$

$$A = S \sin^2 \theta + P \cos^2 \theta \quad (2.31)$$

$$B = RL \sin^2 \theta + PS(1 + \cos^2 \theta) \quad (2.32)$$

$$C = PRL \quad (2.33)$$

Equation 2.30 is biquadratic – we can solve for $\eta^2 = k^2 c^2 / \omega^2$ using the quadratic formula.

Finally, it is worth noting that when considering a single-species plasma (e.g., electrons only), equation 2.30 reduces to the well-known single-species *Appleton-Hartree Equation* (Appleton (1932)):

$$\eta^2 = 1 - \frac{\frac{\omega_{pe}^2}{\omega^2}}{1 - \frac{\omega_{ce}^2 \sin^2 \theta}{2(\omega^2 - \omega_{pe}^2)} \pm \left[\left(\frac{\omega_{ce}^2 \sin^2 \theta}{2(\omega^2 - \omega_{pe}^2)} \right)^2 + \frac{\omega_{ce}^2}{\omega^2} \cos^2 \theta \right]^{1/2}} \quad (2.34)$$

The dispersion relation in equation 2.30 reveals a wealth of information about the characteristics of waves in plasmas. For various plasma densities and background magnetic field strength, we can infer which wave frequencies may propagate, if any, and which wave polarizations. Through the remainder of this work, we will be concerned with the *whistler* mode – a right-hand, circularly-polarized (RHCP) wave. Within a typical magnetospheric plasma, the whistler mode spans the VLF band, roughly between 30 Hz and 300 kHz.

It is difficult to gain much insight directly from the dispersion relation (equations 2.30 or 2.34). However, we can plot the spatial vs temporal frequencies for a fixed angle with respect to the background magnetic field, known as an ω -K diagram, to reveal the various modes of propagation.

Figure 2.4 shows a typical dispersion relation for a magnetospheric plasma ($L \approx 2$) by plotting frequency vs wavenumber ($\eta = kc/\omega$). The whistler mode is the lower branch of the RHCP mode.

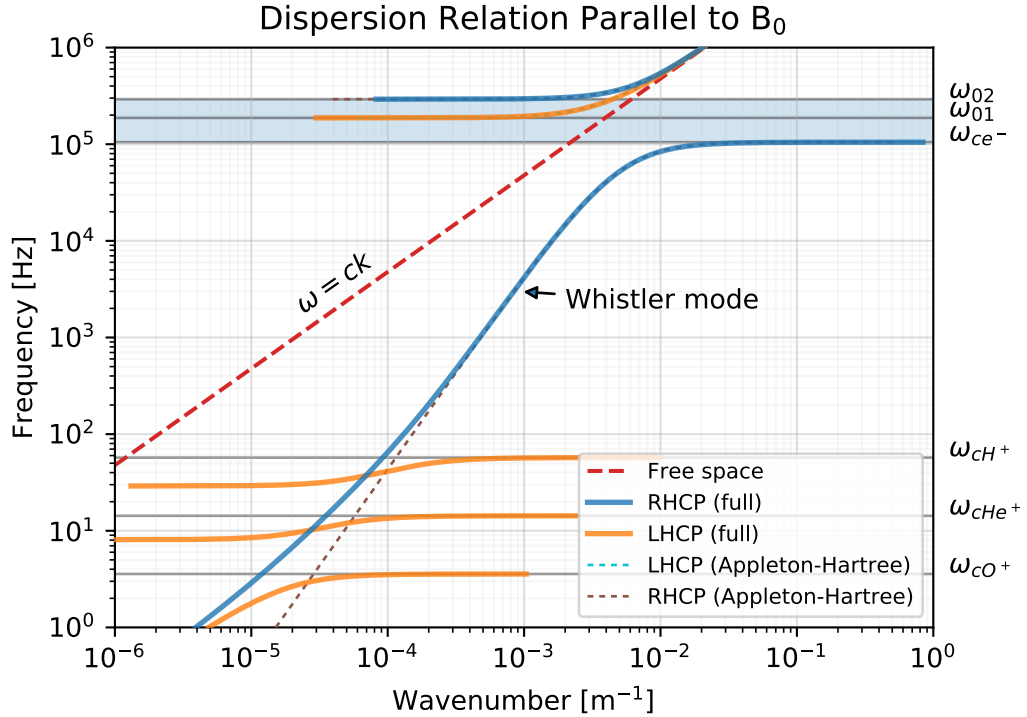


Figure 2.4: An ω -K diagram for the cold plasma dispersion relation, shown here for a wave propagating parallel to \mathbf{B} , in four-component plasma with $N_e \approx 6 \times 10^8 \text{ e}^-/\text{m}^3$, and $B \approx 4 \mu\text{T}$. For higher frequencies the dispersion relation asymptotes to the free-space solution, with slope c . The whistler mode is the right-hand, circularly-polarized mode which spans the majority of the frequency band. The shaded region marks the characteristic band in which the right-hand mode cannot propagate. At lower frequencies, the left-hand circular mode resonates with the various ion constituents, known as the *Ion Cyclotron* modes.

2.2 Ray Tracing and Landau Damping

2.2.1 Ray Tracing

Whistler-mode waves in the magnetosphere propagate for very large distances, and with relatively little attenuation. Under certain conditions, these waves can persist from a few seconds to 1 or more minutes. Simulating the propagation of these waves using a full-wave method would be extremely intractable with current computational resources. However we can use ray tracing to approximate their behavior.

Ray tracing is a technique from geometric optics which tracks the position and velocity of a coherent wave packet – essentially, approximate the behavior of a wave packet to that of a photon, and evaluate the packet’s velocity and wavenormal vector with respect to time. Ray tracing is best suited for coherent, monochromatic wave packets, with no attenuation, dispersion, or mode coupling.

Ray tracing was first applied to the Whistler mode by *Haselgrove* (1954) using a graphical technique, then subsequently by *Haselgrove and Haselgrove* (1960) and *Kimura* (1966) for numerical computation. These papers worked in curvilinear coordinates with respect to a magnetic field line. Haselgrove’s Equations have been used extensively by numerous magnetospheric scientists (*Kimura*, 1966; *Edgar*, 1972; *Ngo*, 1989; *Jasna*, 1993; *Lauben*, 1998; *B.Peter*, 2007; *Bortnik*, 2005; *Kulkarni*, 2009), several using the so-called “Stanford Ray Tracing Program” – a legacy Fortran code which evaluated the Haselgrove equations in two dimensions. Our work uses a slightly different code originally developed by Dr. Forrest Foust (*Golden et al.*, 2010), and is designed for flexibility with respect to plasma density and magnetic field models. Rather than work in curvilinear coordinates with explicit derivatives, we adopt a more-general formulation, using a three-dimensional Cartesian frame and numerically-evaluated derivatives.

We begin with the fundamental ray-tracing equations, as given by *Haselgrove and Haselgrove* (1960); *Stix* (1992):

$$\frac{d\mathbf{r}}{dt} = \frac{\nabla_k F}{\partial F / \partial \omega} \quad (2.35)$$

$$\frac{d\mathbf{k}}{dt} = \frac{\nabla_r F}{\partial F / \partial \omega} \quad (2.36)$$

$$(2.37)$$

Constrained such that:

$$F = F(\mathbf{r}, t, \mathbf{k}, \omega) = 0 \quad (2.38)$$

Equation 2.35 is simply $\frac{\nabla_k F}{\partial F / \partial \omega} \approx \frac{\partial F / \partial k}{\partial F / \partial \omega} = \frac{\partial \omega}{\partial k} = v_g$, the group velocity of a wave packet. The corresponding equation describing the evolution of the wavenormal vector (2.36) is less intuitive, although an analogy can be drawn to Hamiltonian mechanics, in which ω represents a velocity, and k a momentum.

The function F , our “conserved quantity”, is simply the cold plasma dispersion relation given by equation 2.30.

The raytracing equations are a set of coupled, first-order differential equations; solutions to which require some subtlety, but can be addressed using standard numerical techniques.

First, note that we can solve the set at a given time, then evolve the system forward some finite time step. However, the constraint $F = 0$ may not be strictly held afterward. We assert that the error in this constraint must be small; which in turn implies that the background medium must be smoothly-varying – i.e., changing on a spatial scale much greater than our forward step, and of the wavelength of interest. This assumption is known as the *WKB Approximation*.

Adaptive Timestepping

The process of raytracing, then, is to 1) solve the dispersion relation (2.30) to find the refractive index; 2) compute the velocity vector and step the system forward in time; and 3) re-evaluate at the new position to assure that the condition $F=0$ is satisfied. However, properly selecting the timestep is of critical importance – too large a timestep and positional errors will accumulate, or the ray will slip out of a

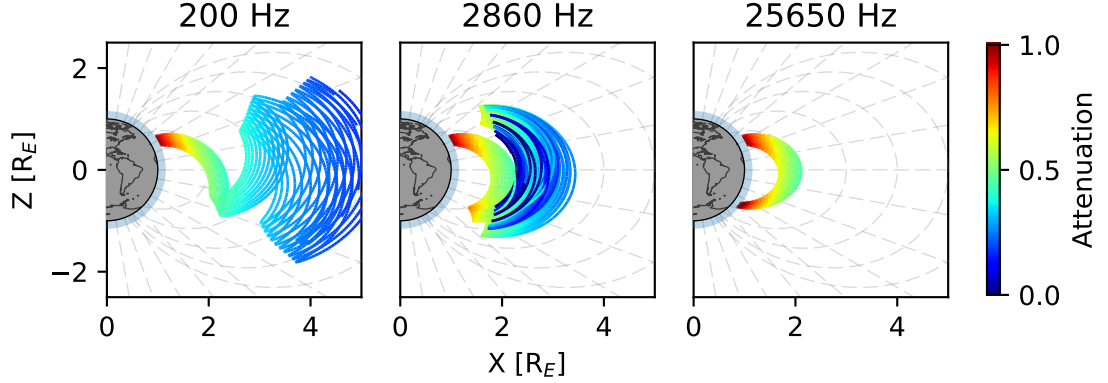


Figure 2.5: Example ray families as computed by the raytracer

propagating mode; too small and computational speed and memory usage suffers. We use an adaptive *Runge-Kutta-Fehlberg* (RK45) (Fehlberg, 1969; Mathews and Fink, 2004) method to continuously update the timestep as the raytracer progresses. RK45 is a common technique for solving ordinary differential equations.

The RK45 method approximates a solution with an initial stepsize dt using two spline fits: a fourth-order and a fifth-order. The error in the step is taken to be the difference between the two estimates. If the error is above a specified tolerance ϵ , the stepsize is reduced and the evaluation is repeated. Additionally, if the error is below a specified tolerance ($\epsilon/10$ in our implementation), the stepsize is increased. The result is a variable time axis with finer resolution in regions of high variability, while enabling longer timesteps in smooth regions for computational efficiency. See appendix B for a detailed description of the Runge-Kutta method.

2.2.2 Landau Damping

The cold-plasma formulation of raytracing described above evaluates the trajectory and wavenormal angle of a wave packet. However, it assumes zero attenuation of wave energy. While it is possible to account for wave attenuation in ray tracing using warm plasma corrections (Sazhin, 1993; Henyey, 1980), we follow the same approximation as used in the legacy ray tracing code, and calculate attenuation along the cold-plasma

raypath according to Landau damping.

Landau damping, originating in a seminal work by *Landau* (1946), is a resonant interaction between a wave and the distribution of electrons and ions comprising the background medium. The Landau mechanism is an interaction with parallel streaming particles and the wave's electric field. Resonant particles are accelerated or decelerated by the wave's electric field; if a majority of the resonant electrons have velocities slightly below that of the wave, then a coherent effect exists, the wavefront imparts some net energy to the plasma, and the wave is attenuated. Conversely, if the majority of resonant particles are moving faster than the wave, some of their energy can be imparted to the wavefront, inducing *wave growth* (*Chen*, 1983; *Kulkarni*, 2009).

Landau damping can have multiple resonances (in which the particle has multiple complete rotations per rotation of the wave). The lowest resonant mode is known as the *Landau* resonance, while the ± 1 modes are referred to as the *Cyclotron* resonances. Higher-order modes remain nameless.

We use the expressions for Landau damping as formulated by *Brinca* (1972). *Brinca* derived expressions for Landau damping assuming a cold background plasma with a sparse warm distribution added, for Whistler waves propagating at an arbitrary angle to the background magnetic field. Inputs to this formulation are the familiar Stix parameters (equations 2.26 - 2.27), which are in turn a function only of location and wave frequency; the wavenormal angle with respect to the background magnetic field; and a distribution function which specifies the energies (and thus velocities) of thermal electrons. The full set of Landau damping equations is given in appendix A.1.

Interestingly, *Brinca's* work was motivated by measurements of Whistler-mode wave growth, rather than attenuation. Our implementation follows suit, and is equally capable of returning growth or damping, depending on the plasma model used. However, throughout this research, wave growth has been exceedingly rare.

Thermal electron distributions

The extent to which a wave is amplified or damped is heavily dependent on the energy distribution of background electrons. The energy distribution, or temperature profile, is specified as a normalized function in phase space – a function of position and velocity, which is normalized to 1:

$$f = f(\mathbf{r}, \mathbf{v}, t) \quad (2.39)$$

$$= f(\mathbf{r}, v_{\perp}, v_{\parallel}, t) \quad (2.40)$$

$$\int_0^{\infty} f dv_{\perp} = 1 \quad (2.41)$$

$$(2.42)$$

Two distribution functions are used in similar work – the *Bell* (2002) distribution, which was derived from POLAR spacecraft measurements of the inner plasmasphere, and the *Bortnik et al.* (2007) distribution, which is based on CRRES spacecraft measurements above $L \approx 7$.

We use the phase space density function as described in *Golden et al.* (2010), which smoothly transitions between the *Bell* (2002) model inside the plasmapause, and the *Bortnik et al.* (2007) model outside the plasmapause. Figure 2.6 shows an example of the distribution function.

2.3 Lightning Illumination Model

A single lightning flash is a stochastic dielectric breakdown process. While a terrestrial lightning flash consists of several repeated strokes at varying incident angles, we adopt the simplified model used by *Lauben* (1998), *Bortnik* (2005), and subsequent workers, and encapsulate the entire discharge process in a single return stroke.

The lightning flash is modeled as a single, vertical current pulse from a height H_E , with a double-exponential time profile given by equation 2.43. The double-exponential current profile is simple and common in the literature, originating with

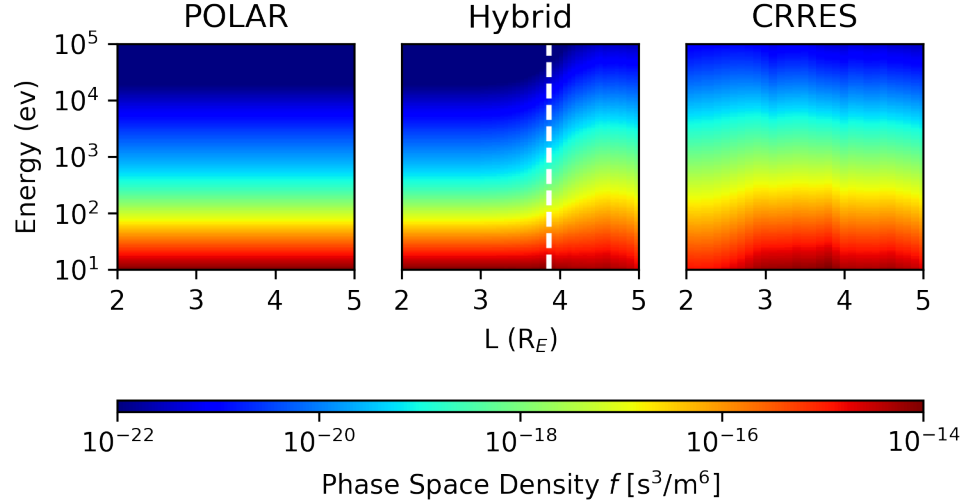


Figure 2.6: Example phase-space density functions, shown for $A_e=1.6$, $K_p=4$, $\alpha=45^\circ$, and $MLT=18$. The POLAR model is used inside the plasmapause, and the CRRES model outside the plasmapause. The hybrid model smoothly transitions between the two. The plasmapause, at $L \approx 4$, is marked by the dashed white line.

Bruce and Golde (1941):

$$I(t) = I_0(e^{-at} - e^{-bt}) \quad (2.43)$$

We relate the time-domain current profile to radiated power using the far-field approximation for an arbitrary source, given by *Griffiths (1999)*, page 457:

$$S(t) \frac{1}{\mu_0} (\mathbf{E} \times \mathbf{B}) = \frac{\mu_0}{16\pi^2 c} [\ddot{p}(t)]^2 \left(\frac{\sin^2 \theta}{r^2} \right) \hat{\mathbf{r}} \quad (2.44)$$

where $p(t)$ is the dipole moment given by $p = 2H_E \int_0^t I(t) dt$, r is the distance from the flash in meters, and θ is the angle to the flash. Taking the second derivative of the dipole moment (the first derivative of the current profile) gives us the far-field time-domain power equation:

$$S(t) = \frac{1}{Z_0} \left(\frac{\mu_0 H_E I_0}{2\pi} \right)^2 \left(\frac{\sin^2 \theta}{r^2} \right) (ae^{-at} - be^{-bt})^2 \hat{\mathbf{r}} \quad (2.45)$$

where we have used the relation $Z_0 = \mu_0 c$. Equation 2.45 gives energy flux density in units of Watts per square meter ($J/m^2/sec$).

To determine the frequency spectrum of the radiated power, we take the Fourier transform of equation 2.45:

$$S(\omega) = \frac{1}{Z_0} \left(\frac{\mu_0 H_E I_0}{2\pi} \right)^2 \left(\frac{\sin^2 \theta}{r^2} \right) \frac{\omega^2 (a-b)^2}{\pi(\omega^2 + a^2)(\omega^2 + b^2)} \hat{\mathbf{r}} \quad (2.46)$$

which gives spectral energy flux, in units of $J/m^2/Hz$.

Throughout this work we assume a flash height $H_E = 5$ km, and model parameters $a = 5 \times 10^3 \text{ sec}^{-1}$ and $b = 1 \times 10^5 \text{ sec}^{-1}$, resulting in a spectrum peaked at approximately 4 kHz; any lightning flash can be parameterized solely by its peak current I_0 and its location on the surface of the Earth. Figure 2.7 shows the current profile and associated spectrum.

The total energy released in a single discharge is determined by integrating equation 2.45 over time and a half-sphere surface:

$$E = \int_{t=0}^{\infty} \int_{\phi=0}^{2\pi} \int_{\theta=0}^{\pi} S(t) r^2 \sin \theta \, d\theta \, d\phi \, dt \quad (2.47)$$

$$= \frac{1}{Z_0} \left(\frac{\mu_0}{2\pi} \right)^2 \frac{(a-b)^2}{2(a+b)} \frac{4\pi}{3} H_e^2 I_0^2 \quad (2.48)$$

$$\approx 1.9 \times 10^{-14} H_e^2 I_0^2 \text{ [Joules]} \quad (2.49)$$

2.4 Trans-Ionosphere Attenuation

The ionosphere, extending from ~ 85 km to 1000 km, is a region of high variability, and a significant factor in the LEP process. As discussed earlier, the majority of VLF energy emitted by a lightning flash propagates efficiently in the Earth-Ionosphere waveguide; however a fraction of emitted energy can propagate upwards through the ionosphere, where the wave experiences significant losses via Joule heating in the D-region ionosphere (*Graf et al.*, 2013; *Blaes et al.*, 2016).

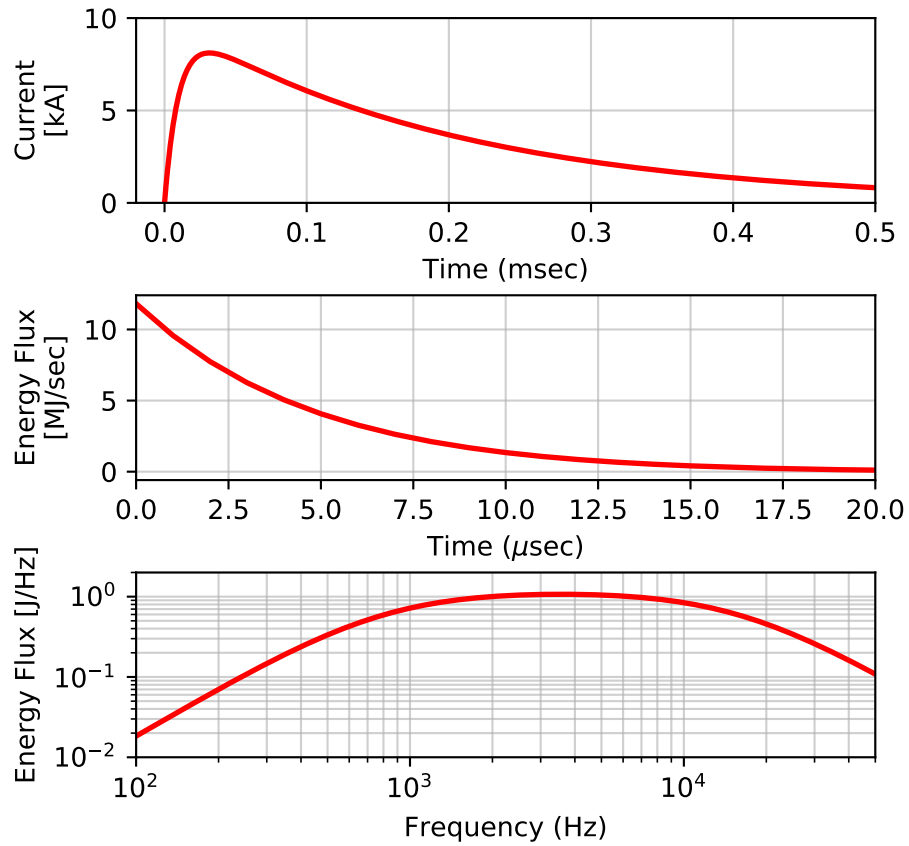


Figure 2.7: Double-exponential current pulse model of a lightning stroke. The top panel shows the stroke current vs time; the middle panel shows the total energy flux, integrated over space, vs time; the bottom panel shows the energy flux in the frequency domain.

Propagation through the ionosphere is ill-suited for a raytracing approach, as in section 2.2, for several reasons: first, the ionosphere electron density varies significantly across a relatively thin slab, effectively violating the WKB (smoothly-varying) approximation. Second, the Landau calculations used to compute ray damping are designed for warm, but collisionless plasmas; the ionosphere is collisional, and only partially ionized, requiring different treatment.

Ionospheric propagation is further complicated by reflection and transmission at the lower boundary layer, as well as mode-coupling between incident plane waves, the whistler mode, and various others.

For computational simplicity, and to more-easily generalize to a variety of conditions, we treat the ionosphere as a single absorbing slab, ranging from 100 to 1000 km in altitude. We assume that waves propagate directly upwards (normal to the Earth’s surface), and are not deflected by ionospheric irregularities or the inclination of the background magnetic field.

Numerous researchers (*Lauben*, 1998; *Bortnik*, 2005; *Kulkarni*, 2009; *Graf et al.*, 2013) have used the classic “Helliwell” curves, taken from *Helliwell* (1965), figure 3-35. Helliwell performs an analysis similar to Landau damping – first deriving a dispersion relation for a collisional plasma, then separating out the imaginary component, which will result in a real-valued attenuation term. The resulting attenuation term is dependent on electron density as a function of altitude, which was extrapolated from sounding rocket campaigns for day and night. The net attenuation is then computed by integrating from 65 to 1500 km in altitude.

Helliwell’s curves have persisted as the default record of trans-ionospheric attenuation; however it has been shown that Helliwell’s curves overestimate trans-ionosphere attenuation by 10 to 20 dB (*Starks et al.*, 2008), due mainly to the coarse measurement of the ionosphere electron density profile.

Rather than Helliwell’s curves, we use results from *Graf et al.* (2013), which are derived from extensive full-wave simulations using the International Reference Ionosphere (IRI) plasma density profile. Related work using the same full-wave model has been experimentally verified at ~ 20 kHz using DEMETER satellite measurements of VLF transmitters (*Cohen et al.*, 2012). *Graf et al.* reports a set of curves in the same

manner as Helliwell – power attenuation as a function of latitude, for two frequencies (2 kHz and 20 kHz), for dayside and nightside ionospheres. We then interpolate (or extrapolate) in log-space to find an attenuation factor for any latitude or frequency of interest ($\approx 10^\circ - 70^\circ$, and 200 Hz - 30 kHz).

We transition between the dayside and nightside attenuation curves using a Sigmoid function, with an approximate 1-hour transition width.

Figure 2.8 compares the *Graf et al.* (2013) and *Helliwell* (1965) attenuation curves, which model the integrated wave power losses between 65 km - 1500 km altitude as a function of frequency and geomagnetic latitude. Both models exhibit similar trends – higher attenuation towards the equator, and higher attenuation on the dayside – however the Helliwell curves report significantly greater attenuation overall. We can attribute this due to the electron density profile used in their calculation.

2.5 Wave-Particle Interactions

A trapped particle follows a fixed trajectory, bouncing indefinitely back and forth between its reflection points at the northern and southern hemispheres. The particle’s local pitch angle varies with latitude; however in the absence of external interactions, the pitch angle remains the same at each pass. For convenience, we can relate any local pitch angle back to the equatorial pitch angle through conservation of the first adiabatic invariant (2.4).

$$\sin^2 \alpha(\lambda) = \frac{B(\lambda)}{B_{eq}} \sin^2 \alpha_{eq} \quad (2.50)$$

A trapped particle’s equatorial pitch angle remains a constant of the motion. However, it can be altered by means of a perturbation to the local magnetic field. Generally, small perturbations will be incoherent, and have negligible net effect on a particle’s trajectory when compared to the background magnetic field. In the case of resonant wave-particle interactions, the particle’s gyrorotation and the wave’s magnetic field can be coherent, and have a significant effect on the particle’s trajectory.

An essential characteristic of resonant wave-particle interactions is that while some

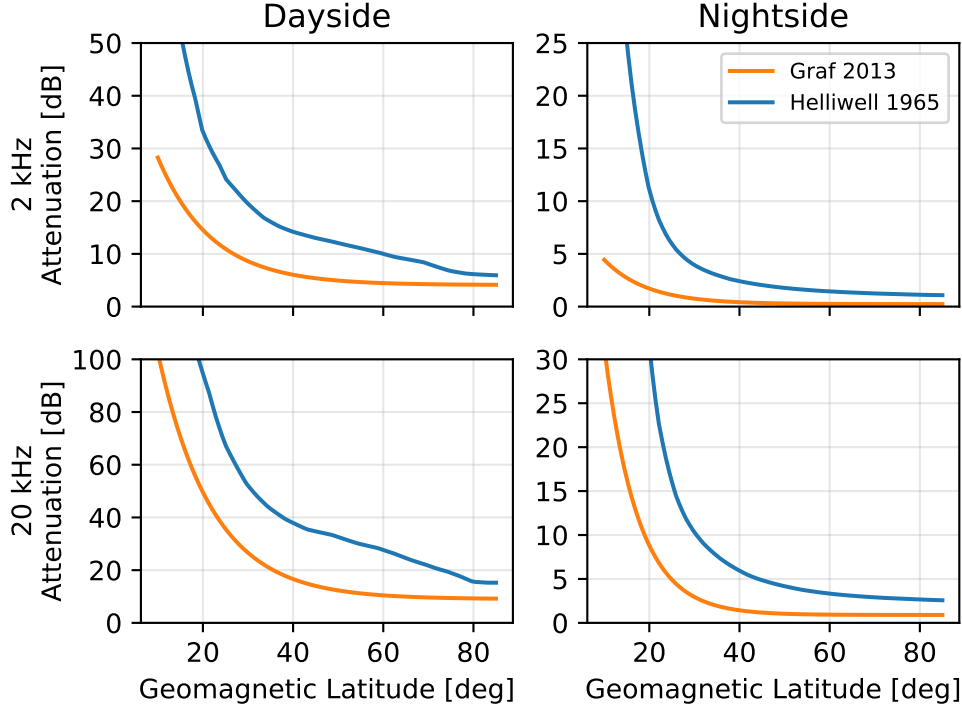


Figure 2.8: Trans-Ionosphere attenuation curves for the dayside and nightside, at 2 kHz and 20 kHz. Reproduced from *Graf et al.* (2013), figure 7. The *Graf et al.* curves show markedly less attenuation than the previously-used *Helliwell* curves, especially at equatorial latitudes, and on the day side.

energy can be imparted through the wave’s electric field, no energy is exchanged through the magnetic field – rather, the perturbative effect of the wave magnetic field primarily shifts the particle’s own kinetic energy between the parallel and perpendicular modes (v_{\parallel} , v_{\perp}).

2.5.1 Resonant Interactions

We begin by considering the resonant interaction between a monochromatic, elliptically-polarized wave, propagating obliquely (i.e., not strictly aligned with the background magnetic field). We can then calculate the resonant, doppler-shifted perturbative fields \mathbf{E}_w , \mathbf{B}_w , and calculate the change to a test particle’s momentum using the

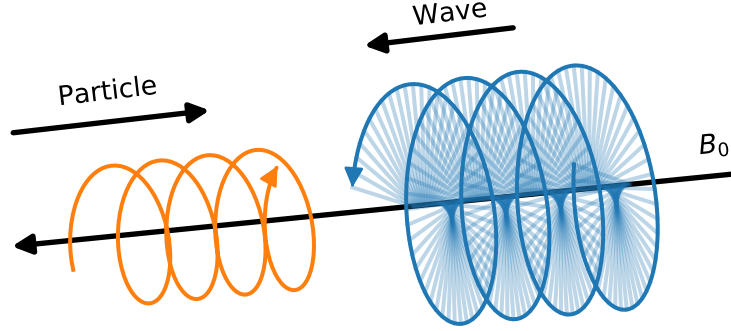


Figure 2.9: An illustration of a counter-streaming wave-particle interaction. At resonance, a gyrating particle sees an effective constant electric and magnetic field. Resonant interactions can occur in co-streaming (same direction) or counter-streaming (opposite direction) encounters.

relativistic Lorentz force. This analysis stems from *Bell* (1984), and has been used in numerous successive studies – *Jasna* (1993); *Lauben* (1998); *Bortnik* (2005), and others.

The condition for resonance is given by *Chang and Inan* (1983):

$$\frac{d\eta}{dt} = \omega + v_z^{res} k_z - m\omega_c/\gamma \approx 0 \quad (2.51)$$

where η is the angle between the right-hand circular component of the wave magnetic field (B_r) and the resonant particle's perpendicular velocity vector (v_\perp), ω is the wave frequency, $m \in \mathbb{Z}$ is the resonance order, and $\gamma = (1 - (v^{res}/c)^2)^{-1/2}$ is the relativistic correction factor.

We use the *Bell* (1984) expression for change in pitch angle with respect to time, corrected for relativistic factors by *Jasna* (1993); *Bortnik et al.* (2006):

$$\frac{d\alpha}{dt} = \frac{m_e \omega_{\tau m}^2}{k_z p_\perp} \left(1 + \frac{\cos^2 \alpha}{m \omega_c / \omega - 1} \right) \sin \eta + \frac{1}{m_e \gamma} \frac{p_\perp}{2\omega_c} \frac{\partial \omega_c}{\partial z} \quad (2.52)$$

with the following parameter definitions:

$$\beta = \frac{k_x p_\perp}{m_e \gamma \omega_c} \quad (2.53)$$

$$k_z = k \cos \theta = (\omega \mu / c) \cos \theta; \quad k_x = k \sin \theta \quad (2.54)$$

$$\omega_{\tau m}^2 = (-1)^{m-1} \omega_{\tau 0}^2 [J_{m-1}(\beta) - \alpha_1 J_{m+1}(\beta) + \gamma \alpha_2 J_m(\beta)] \quad (2.55)$$

$$\omega_{\tau 0} = \frac{\omega_1 k_z p_\perp}{\gamma m_e} \quad (2.56)$$

$$\omega_1 = \frac{e}{2m_e} (B_x^w + B_y^w); \quad \omega_2 = \frac{e}{2m_e} (B_x^w - B_y^w) \quad (2.57)$$

$$\alpha_1 = \frac{\omega_2}{\omega_1} \quad (2.58)$$

$$\alpha_2 = \frac{e E_z^w}{\omega_1 p_\perp} \quad (2.59)$$

$$R_1 = \frac{E_x^w + E_y^w}{B_x^w + B_y^w}; \quad R_2 = \frac{E_x^w - E_y^w}{B_x^w - B_y^w} \quad (2.60)$$

where e and m_e are the electron charge and rest mass, p_\perp is the perpendicular component of the particle's momentum, J_i are Bessel functions of the first kind, and $E_{x,y,z}^w$, $B_{x,y,z}^w$ are the vector components of the incident wave, oriented such that the z-component is parallel to the background magnetic field.

A full derivation of equations (2.52) - (2.60) is beyond the scope of this dissertation; however the full derivation is explained in the theses of *Bortnik* (2005), *Jasna* (1993), and *Bell* (1984).

While the full set of equations (2.52) - (2.60) is complex, we can identify several broad trends: First, $\partial \alpha / \partial t \propto \sin \eta$, which implies that, when the resonance condition is not met, oscillating changes will have no cumulative effect. Second, $\partial \alpha / \partial t \propto \alpha$, which increases the complexity of the solution space; however we can introduce a simplification by assuming that changes in pitch-angle are small, and therefore only particles with pitch angles very near the loss cone will be of significance. We can therefore introduce a relationship between pitch angle and v_\perp and p_\perp (*Bortnik et al.*, 2006):

$$v_z^{res} = \frac{\pm \sqrt{\omega^2 k_z^2 + [(m\omega_c)^2 - \omega^2][k_z^2 + (\frac{m\omega_c}{c \cos \alpha_{lc}})^2]} - \omega k_z}{k_z^2 + (\frac{m\omega_c}{c \cos \alpha_{lc}})^2} \quad (2.61)$$

2.5.2 Recovering Wave Amplitudes from Poynting Flux

Required in our modeling is the ability to link the results of raytracing to the wave-particle interaction model. However, raytracing tracks only coarse-grained wave parameters – wavenormal vector, propagation angle with respect to the background magnetic field, and the background plasma parameters. We use the formulation from *Bell* (1984), which has since been used by *Jasna* (1993); *Lauben* (1998); *Bortnik et al.* (2006), to relate the Poynting flux and the individual wave components B_x^w, B_y^w, B_z^w .

Starting from the definition of Poynting flux $\mathbf{S}^w = (1/2)\text{Re}(\mathbf{E}^w \times \mathbf{H}^w)$, *Bell* (1984) finds a relation to a single magnetic field component, B_y^w :

$$\|B_y^w\| = \frac{2\mu_0 \rho_2^2 X^2 \eta \cos \theta \|\mathbf{S}^w\|}{c \sqrt{(\tan \theta - \rho_1 \rho_2 X)^2 + (1 + \rho_2^2 X)^2}} \quad (2.62)$$

$$X = \frac{P}{P - \eta^2 \sin^2 \theta} \quad (2.63)$$

$$\rho_1 = \frac{E_z^w}{E_y^w} = \frac{(\eta^2 - S)\eta^2 \sin \theta \cos \theta}{D(\eta^2 \sin^2 \theta - P)} \quad \rho_2 = \frac{E_x^w}{E_y^w} = \frac{\eta^2 - S}{D} \quad (2.64)$$

where ρ_1, ρ_2 are the wave polarization ratios, η is the wave refractive index, θ is the angle between the wavenormal and the background magnetic field, \mathbf{S}^w is the Poynting flux, and S, D, and P are the Stix parameters defined in (2.26) and (2.27).

The remaining five wave components are given by:

$$E_x^w = \frac{\|cB_y^w(P - \eta_x^2)\|}{P\eta_z} \quad (2.65)$$

$$E_y^w = \frac{\|E_x^w D\|}{S - \eta^2} \quad (2.66)$$

$$E_z^w = \frac{\|E_x^w \eta_x \eta_z\|}{\eta_x^2 - P} \quad (2.67)$$

$$B_x^w = \frac{\|E_x^w D \eta_z\|}{c(S - \eta^2)} \quad (2.68)$$

$$B_z^w = \frac{\|E_x^w D \eta_x\|}{c(X - \eta^2)} \quad (2.69)$$

2.6 Environment Models

Within this work, we will encounter several different regions of the space environment – This section provides a collected overview of each region and the models used.

2.6.1 Magnetic Field

Magnetic Dipole To first order, the Earth’s magnetic field can be approximated as a dipole, with origin at the Earth’s center, and a tilt of $\approx 11^\circ$ from the axis of rotation. The dipole model, sometimes referred to as the “centered dipole” or “tilted dipole”, is reasonably accurate for midlatitude field measurements over the continental United States, but can deviate significantly from the true field elsewhere. Similarly, the dipole field model is reasonably accurate for middle latitudes, below ≈ 10 Earth radii, but become increasingly inaccurate at higher latitudes, and at larger distances from the Earth, where the Earth’s internal field is no longer dominant.

The dipole model, however, excels in its simplicity – the dipole magnetic field can be completely described in a closed form, and can be computed rapidly and reliably.

The dipole potential is given by:

$$\psi_{dip} = B_0 \left(\frac{R_e}{r} \right)^2 \cos \theta \quad (2.70)$$

The individual components of the magnetic field are given by the negative gradient of the scalar potential:

$$\mathbf{B} = -\nabla\psi \quad (2.71)$$

$$B_r = -2B_0\left(\frac{R_e}{r}\right)^3 \cos\theta \quad (2.72)$$

$$B_\theta = -B_0\left(\frac{R_e}{r}\right)^3 \sin\theta \quad (2.73)$$

$$B_\phi = 0 \quad (2.74)$$

Within this work we use $B_0 = 31.5 \mu\text{T}$ and $R_e = 6371 \text{ km}$.

A single fieldline, determined by integrating the direction of the field vector, can be described by it's *L-shell* – the fieldline's altitude, in units of Earth radii, measured at the equator.

For the dipole field, the radius of a field line at any latitude is related by:

$$R(\lambda) = R_e L \cos^2 \lambda \quad (2.75)$$

The dipole field can then be used as an orthogonal coordinate system, with any location being specified by a latitude, longitude, and L-shell (*McIlwain*, 1961).

Within the plasmasphere, the dipole model works well. However, closer to the Earth's surface the model becomes increasingly inaccurate, necessitating a higher-order model.

IGRF The International Geomagnetic Reference Field (IGRF) is a 13th-order spherical expansion model, with coefficients updated every few years based on terrestrial measurements (*Thébault et al.*, 2015). Within this work we use the IGRF-12 model as a realistic representation of the Earth's internal magnetic field.

IGRF is quick and simple to calculate at any given location, and is much closer to reality than a simple dipole field. However, due to the added complexity, there are not closed-form expressions for field line trajectories or L-shells, which can make dealing with IGRF (and any higher-order model) more cumbersome.

Figure 2.11 contrasts lines of constant L-shell between the dipole and IGRF models.

Tsyganenko Corrections The dipole and IGRF models represent the Earth’s internally-generated magnetic field. However, as one moves further away from the Earth ($L > \sim 8$), the Earth’s internal field becomes less dominant, and external fields, namely forcing from the solar wind, cannot be ignored. The total field present in the space environment is the sum of both internal and external contributions.

Numerous models of the external field exist; within this work we consider the T05 external field model (*Tsyganenko and Sitnov, 2005*). The external field model exhibits seasonal and daily variation. However, for fieldlines below $L \approx 6$, the external field effects can be ignored.

Figure 2.10 contrasts the dipole, IGRF, and T05-corrected models in the meridional plane; Figure 2.11 illustrates the deviation in fieldline contours along the Earth’s surface between the dipole and IGRF models.

2.6.2 Plasmasphere

The plasmasphere is a region of the space environment surrounding the Earth, and a primary unknown within our modeling. The plasmasphere extends from an altitude of 1000km up to several Earth radii; typically it is divided into two separate regions: a dense, relatively cold *inner plasmasphere*, and a sparse, relatively hot *outer plasmasphere* or *trough*. The transition boundary between the two regions is a sharp dropoff in plasma density called the *plasma pause*.

Much like the ionosphere, the plasmasphere is a highly variable region, depending on solar conditions (K_p), location (latitude, longitude, field line), and time of day (MLT). The large spatial scales, high variability, and sparse availability of in-situ measurements require us to turn to empirical models of each region. We consider three primary models of electron density, and two of electron temperature.

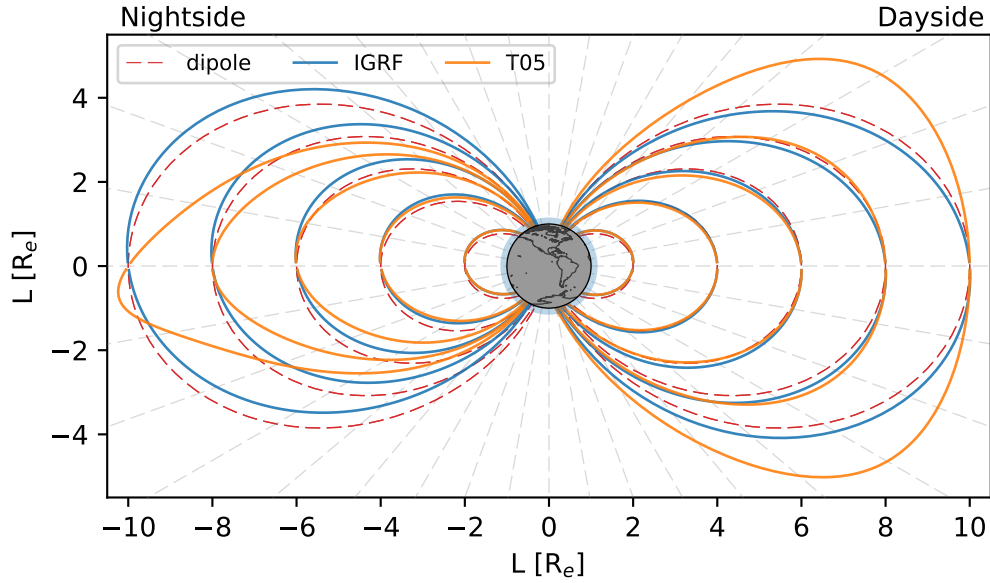


Figure 2.10: Three different magnetic field models, shown in the meridional plane, in geomagnetic coordinates: the tilted dipole, the IGRF model, and the Tsyganenko-Corrected IGRF model. Solar wind is incident on the right side.

Overview of Plasmasphere Density Models

Ngo Model The Ngo model is a legacy model used extensively in research at Stanford from the early 1980s through the mid-2000s, notably by *Lauben* (1998) and *Bortnik* (2005), and has heritage dating back to the early days of radioscience at Stanford (*Kimura*, 1966). The model uses a Diffusive Equilibrium (DE) (*Angerami*, 1963) model for the inner and outer plasmasphere, onto which the *Carpenter and Anderson* (1992) inner plasmasphere model is overlaid. This model was integrated into the legacy Stanford VLF raytracing code, and provided several adjustable parameters, including plasmopause location, constituent ratios, and the ability to include ducts.

Global Core Plasmasphere Model (GCPM) The Global Core Plasmasphere Model, initially developed in 2000 by *Gallagher et al.* (1999) with significant updates through the following decade, smoothly transitions between several regional models

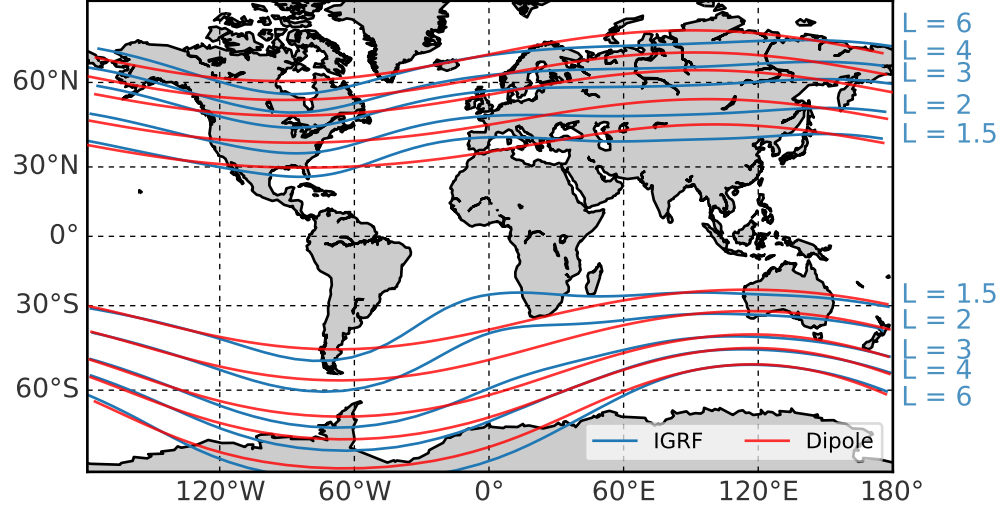


Figure 2.11: Fieldline contours along the Earth's surface, shown for the dipole and IGRF models.

to provide a continuous model of the plasmasphere. Within this work we use version 2.4, which was released in 2009 and made available by the Space Plasma Physics group at the NASA Marshall Space Flight Center (<https://plasmasphere.nasa.gov>). GCPM incorporates the *Carpenter and Anderson* (1992) inner plasmasphere model and the *Gallagher et al.* (1995) outer plasmasphere model, with an empirical fit of the plasmopause location between. The polar cap model is derived from *Persoon et al.* (1983) and *Chandler et al.* (1991). All models are connected smoothly to the IRI model of the ionosphere at lower altitudes. The combined GCPM model is parameterized by K_p and MLT.

Simplified GCPM GCPM aims to provide a dynamic, complete picture of the plasmasphere as a function of time and K_p ; however for our purposes GCPM provides too much variation. Additionally, the combination and smoothing between many models is computationally slow. In order to provide quicker computation and to reduce the number of parameters to adjust, we have implemented a simplified version

of GCPM.

This model uses the equatorial-plane GCPM model, including the plasmopause location. However we omit any variation in electron density along latitude, and assume densities are constant along each field line. As our region of interest lies primarily within low and mid latitudes, we omit the polar cap model altogether and simply merge the ionosphere into the equatorial trough model. Finally to simplify computation, we model the ionosphere using an empirical fit to IRI – one for noon, and one for midnight, with a smooth transition along longitude. Figure 2.12 shows a side-by-side comparison of the three models, for $K_p = 2$.

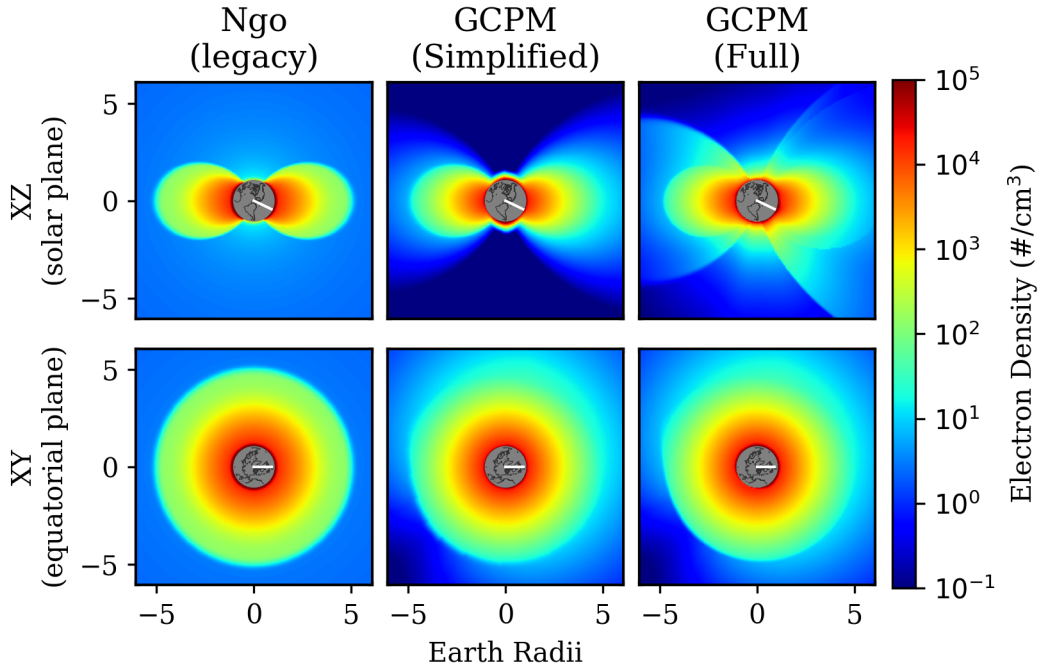


Figure 2.12: A comparison of three plasmasphere models: Ngo, simplified GCPM, and full GCPM, for a relatively quiet plasmasphere ($K_p = 2$). The top row shows electron density in-plane with the direction of solar influx; the bottom row shows a top down (equatorial cross-section) view. The white line indicates the solar axis. Only electron density is shown, as additional plasma constituents are derived from electron density.

2.6.3 Ionosphere

The ionosphere, extending from ≈ 85 km to 1000 km, is the highly-variable transition region between the terrestrial neutral atmosphere and the sparse plasmas of the space environment. In general, our treatment of wave propagation in the ionosphere is abstracted using the method described in section 2.4. However, in raytracing through the plasmasphere, we require a smoothly-varying transition between the plasmasphere and ionosphere models.

IRI The International Reference Ionosphere (IRI) is a standard model of several key plasma parameters – electron density, electron and ion temperatures, ion composition, and so forth. IRI provides detailed outputs as a function of location, altitude, and local time. The GCPM plasma model uses the IRI-2007 implementation (*Bilitza and Reinisch, 2008*); the simplified IRI model is derived from the IRI-2016 model (the most-current available version at time of writing).

Simplified IRI In order to both reduce our model parameter space, and to greatly decrease computation time, we pair a simplified version of IRI with a simplified version of GCPM. The IRI-2016 model was run for dayside and nightside ionospheres (12 and 0 MLT), using all default settings, for January 1st, 2000. We then fit a multiple-Gaussian function to the electron density vs latitude, at an altitude of 1500 km, and at the F_2 peak. Electron density variation with respect to altitude is approximated by a log-linear fit between 1500 km and the F_2 peak. Finally, longitudinal variation is smoothed with a sigmoid function with a width of ~ 1 hr. Figure 2.13 shows both the IRI electron density and the derived curve fits.

2.6.4 The Radiation Belts

Section 2.6.2 describes the density of electrons and ions in the near-Earth environment. Absent from these models, however, is a discussion of electron and ion energies. The model in section 2.2.2 assigns an energy distribution to electrons in the ~ 1 eV range to model a warm plasma.

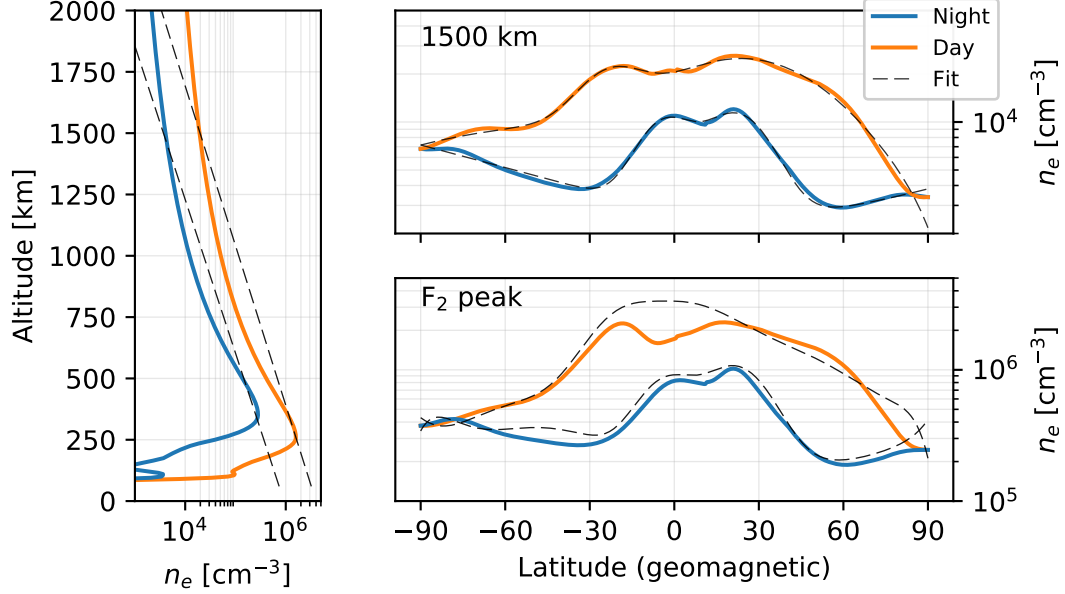


Figure 2.13: The IRI electron density model and derived curve fits. The left panel shows electron density variation as a function of altitude, for day and night. The right panels show electron density variation with respect to latitude, for (top) 1500 km and (bottom) the F_2 peak (approx. 300 km). Dashed lines indicate the fitted curves used by the simplified IRI model.

The term “Radiation Belts” or “Van Allen belts” refer to the trapped distributions of sparse, very-high-energy electrons, which exhibit two shell-like enhancements which comprise the inner and outer radiation belts.

We model the trapped electron population using the AE8 density model (*Vette*, 1991). AE8 provides omnidirectional, integral fluxes of high-energy electrons as a function of L-shell energy. AE8 is the culmination of several decades of radiation belt studies by the National Space Science Data Center (NSSDC), with the first efforts originating with *Vette* (1966). AE8 combines measurements from ~ 94 different instruments across ~ 24 satellite missions from the 1960s and 1970s, which spanned a wide range of orbits, from LEO out to geostationary (*Cayton*, 2005).

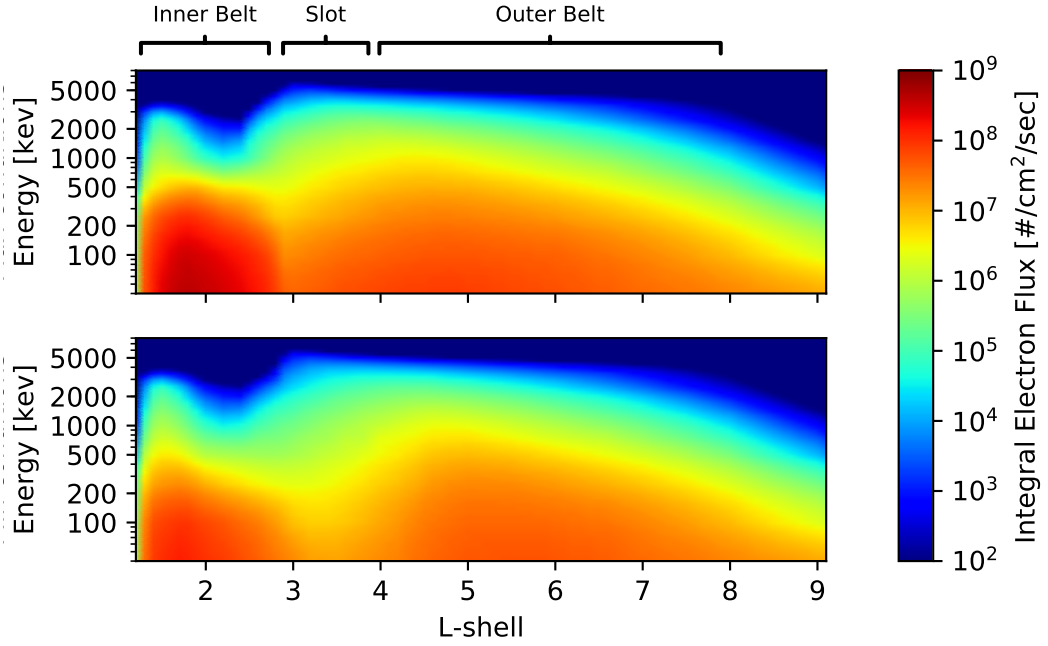


Figure 2.14: Integral flux for energetic electrons in the radiation belts, as reported by the AE8 model (*Vette*, 1991). The top frame shows the model of maximum conditions, and the bottom frame minimum conditions. The two radiation belts are visible as enhancements within $L \approx 2 - 3$ for the inner belt, and $L \approx 4 - 7$ for the outer belt. The belts are separated by a depletion known as the “slot” region.

Figure 2.14 shows the AE8 model output for minimally-populated and maximally-populated conditions.

The AE8 model reports omnidirectional, integral fluxes – that is, the total electron flux integrated over a spherical surface – at the geomagnetic equator. However we require finer detail in directional flux of electrons, which we model via a distribution of pitch angles. *Lauben* (1998) assumed the simplest distribution, with electrons uniformly-distributed in pitch angle up to the loss cone. *Bortnik* (2005) compared the square distribution to a more-realistic, sinusoidal distribution. Here we assume a sinusoidal pitch-angle distribution along with the AE8 flux density model. Figure 2.15 contrasts the square and sinusoidal distribution functions.

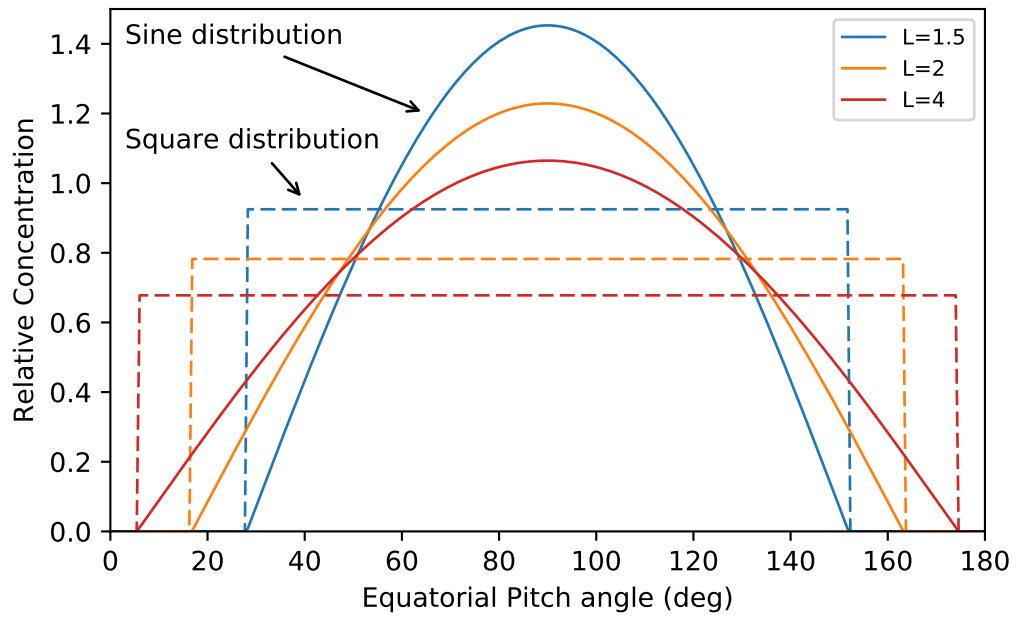


Figure 2.15: Two models of the distribution in pitch angle of radiation belt electrons. The simplest model is a square-shaped distribution, wherein pitch-angles are equally represented within the trapped population. A more realistic model is a sinusoidal distribution. Densities within the loss cone ($\alpha < \alpha_{lc}$) are assumed to be zero.

Chapter 3

VLF energy in the Near-Earth Environment

The purpose of this chapter is to provide a quantifiable assessment of the persistent radio wave energy in the near-Earth space environment due to lightning-generated Whistlers. The morphology of LEP (time evolution, spatial extent at the Earth’s surface, and so forth) are primarily determined by the location of wave-particle interactions; additionally, wave-particle interactions with Whistlers are hypothesized to be the primary cause of slot-region electron depletions, and the “impenetrable barrier” below $L \sim 2$.

Lightning-generated Whistlers are sporadic, and exist alongside a multitude of radio wave activity, such as VLF chorus and plasmaspheric hiss, making a correlated *in-situ* measurement challenging. Within this chapter we simulate the relative VLF energy (L-shell, latitude, longitude) in the near-Earth space environment, in volumetric units [J/m^3], as a means of assessing their relative contribution to the persistent radio spectrum.

3.1 Methodology

Our simulation is divided into two portions: First, a simulation of persistent VLF energy due to a single flash originating at a fixed latitude, and second, an integration

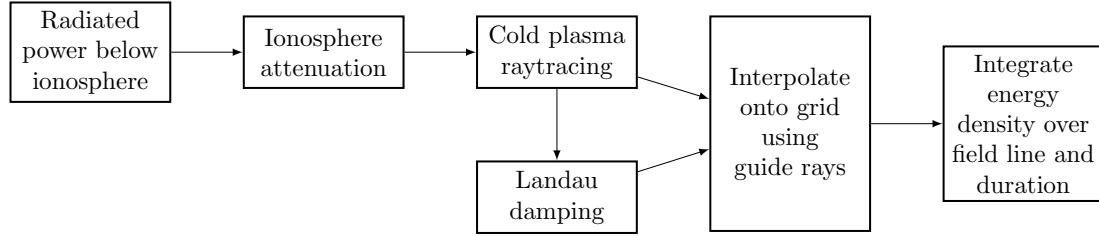


Figure 3.1: Block diagram of the average energy density calculation for a single flash.

over a measured lightning dataset, using scaled and shifted “stencils” for each flash.

Figure 3.1 shows the steps required to compute a single stencil.

1. First we model the sub-ionosphere power spectrum generated from a flash with a known peak current, using the methodology of section 2.3.
2. We then propagate the energies through the ionosphere, using the attenuating slab approximation method of section 2.4.
3. We map the effective power above the ionosphere (J/m^2 at 1000 km altitude) to an energy density along a fixed grid using a set of pre-computed “guide rays” using the methodology in section 2.2, the Landau damping from section 2.2.2, and the novel interpolation scheme described below.
4. In order to account for multiple crossings at each grid point, and to reduce our output space across different latitudes, we store the time-averaged energy density along each field line.

Table 3.1: Simulation Parameters

Latitude spacing	1°
Longitude spacing	1°
Frequency range	200 Hz - 30 kHz
Coarse Frequencies	33 (log-spaced)
Fine Frequencies	20

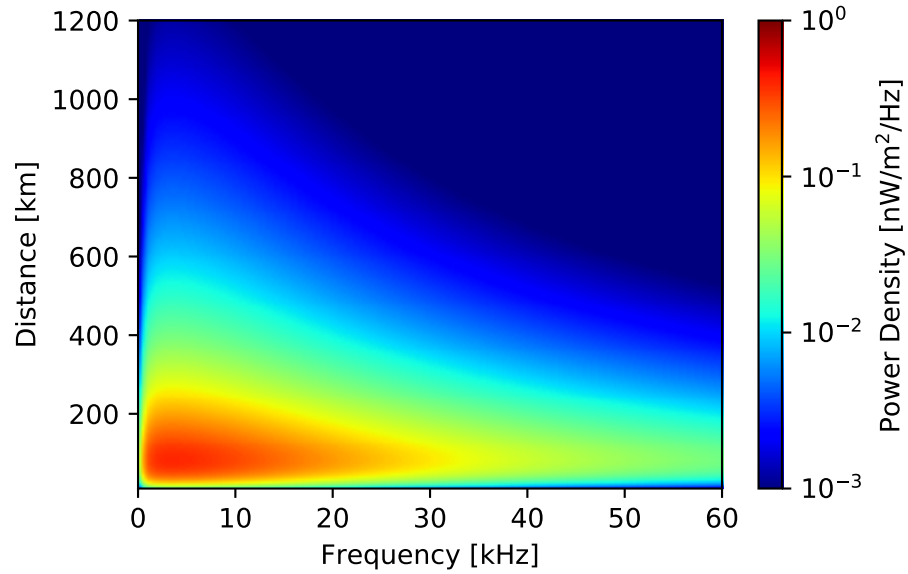


Figure 3.2: Vertically-propagating power density from a single discharge, as a function of frequency and radial distance. Adapted from *Marshall et al.* (2011).

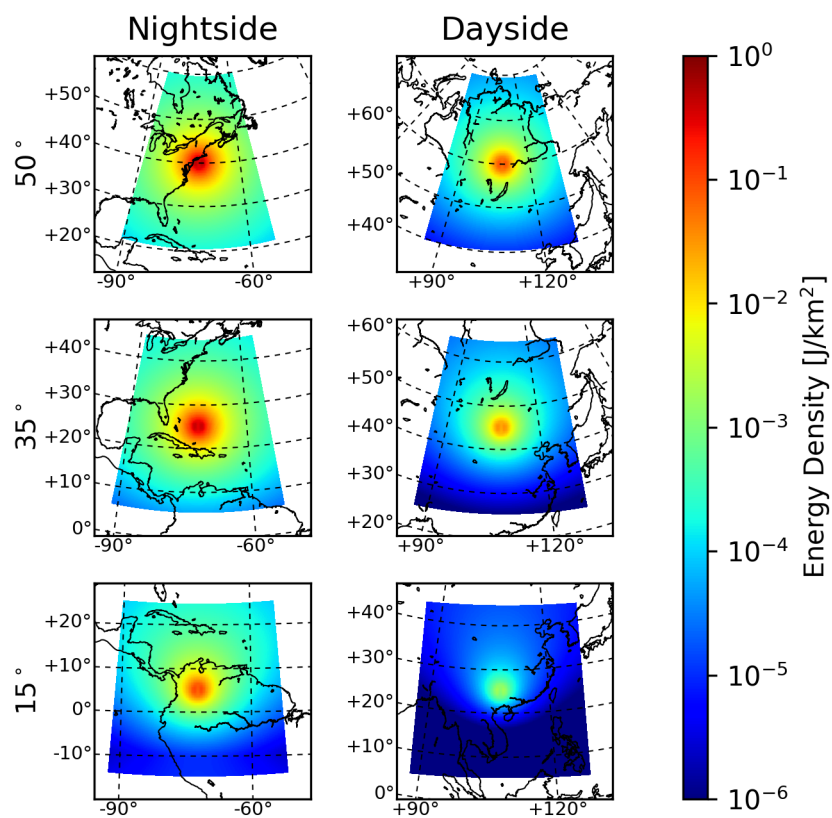


Figure 3.3: Illumination pattern, integrated over frequency, after ionospheric attenuation (altitude = 1000 km).

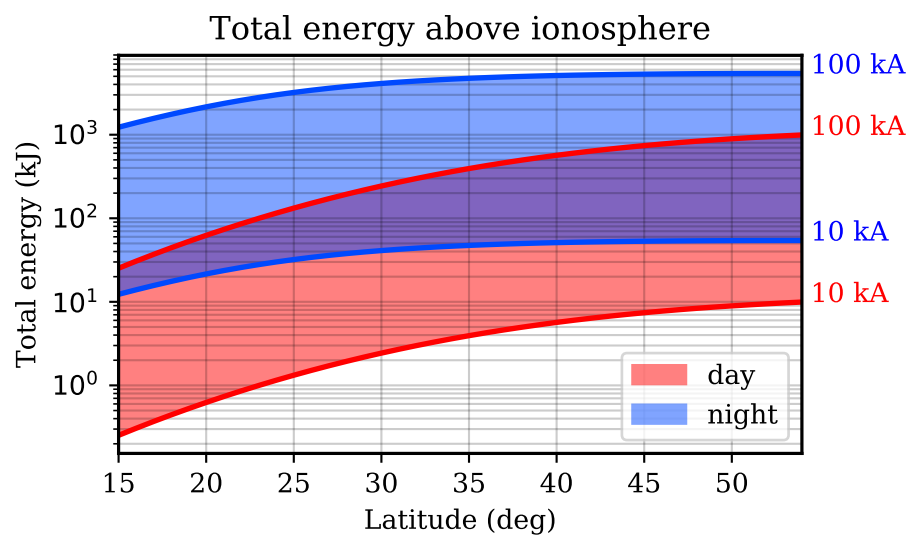
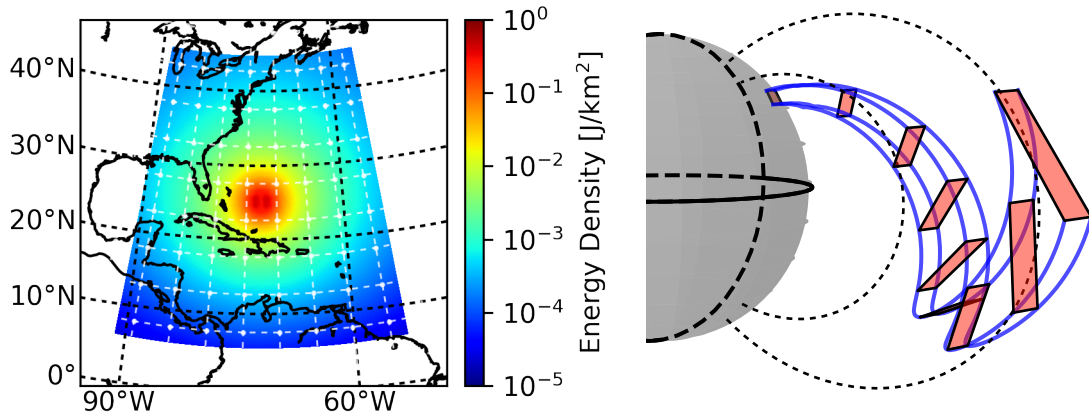


Figure 3.4: Integrated energy above the ionosphere from a single discharge, as a function of geomagnetic latitude. Energy scales quadratically with peak current; totals for 10 kA (an average flash), and 100 kA (a strong, but not unreasonable flash) are overlaid.



(a) Input energy gridding

(b) “guide ray” construction

Figure 3.5: An illustration of the interpolation scheme. (a) Energy at the top of the ionosphere is divided into cells, in latitude, longitude, and frequency. Shown here with 5° cells (much larger than used in simulation). The plotted energy is integrated over frequency. (b) Illustration of the guide ray method. Input energy is integrated between a set of guide rays, spaced in latitude, longitude, and frequency. This energy is then averaged over a 4-dimensional volume, bounded by two adjacent timesteps $t - 1$, t of the guide rays.

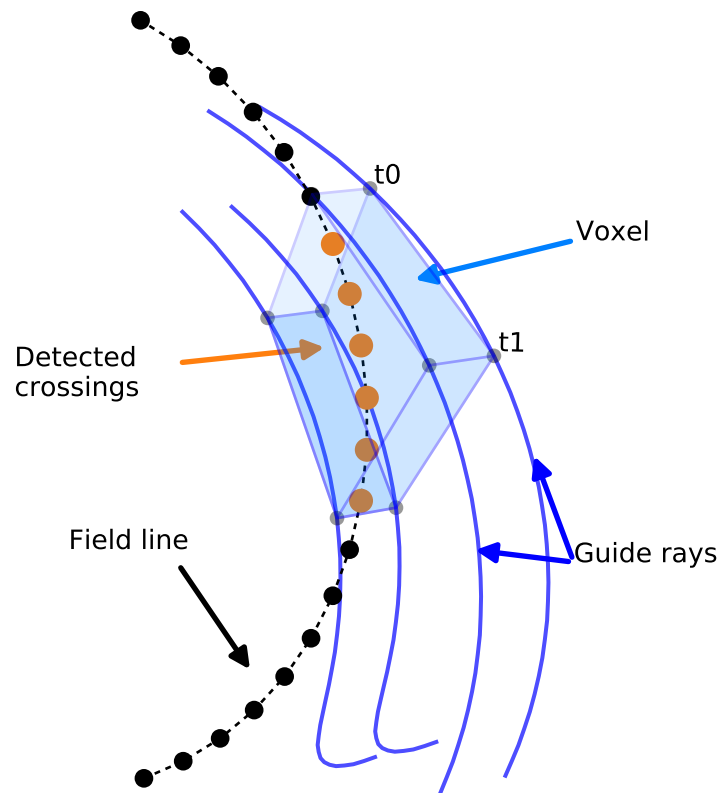


Figure 3.6: Illustration of the Delaunay interpolation method, shown here in three dimensions (e.g., for a single frequency).

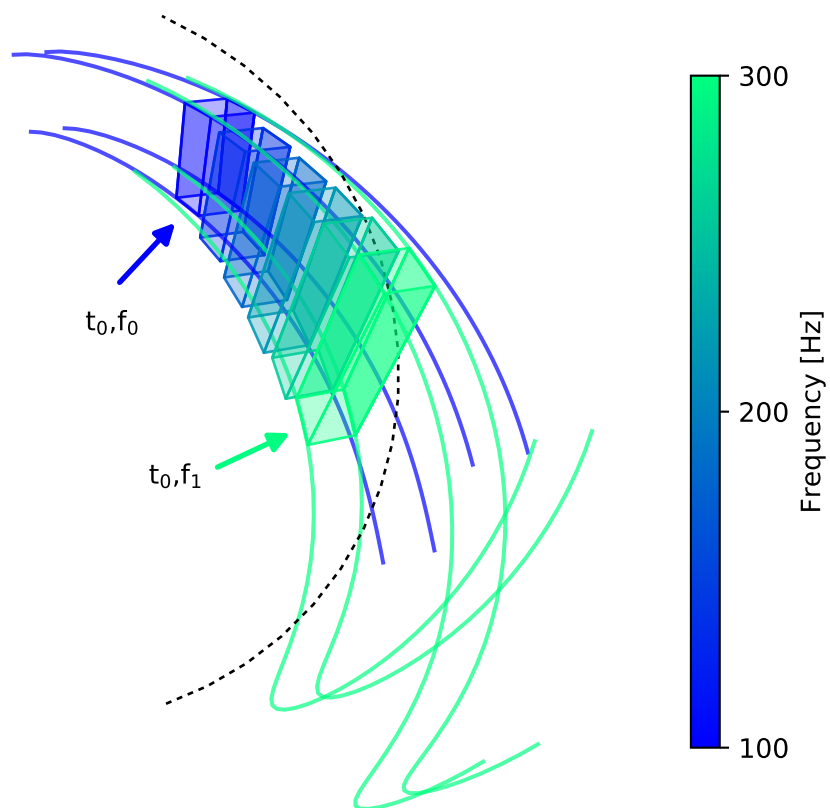


Figure 3.7: Fine-scale frequency interpolation.

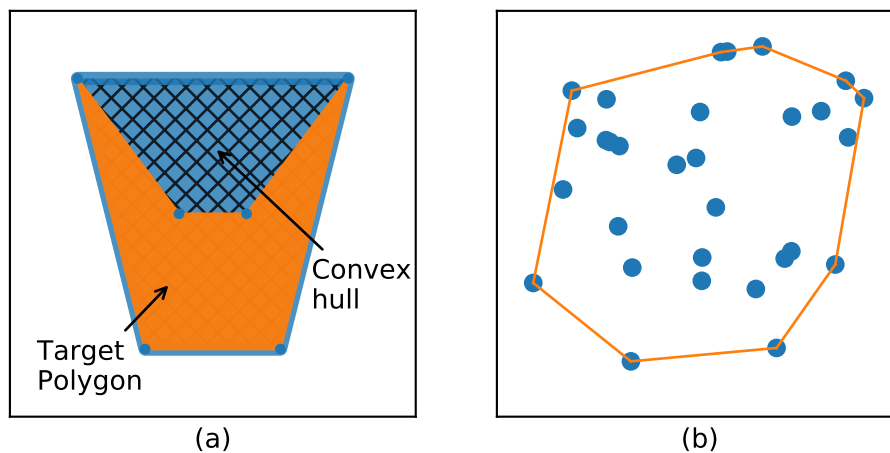


Figure 3.8: Illustration of a convex hull in two dimensions.

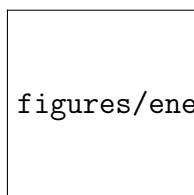


Figure 3.9: Block diagram

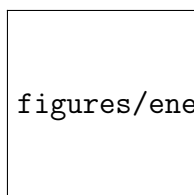


Figure 3.10: Block diagram

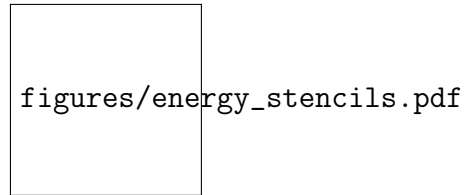


Figure 3.11: Block diagram

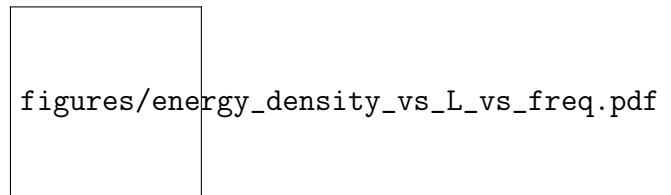


Figure 3.12: Average energy density as a function of L-shell and wave frequency

3.2 Persistent Energy from a Single Flash

3.2.1 Radiated power above the ionosphere

3.2.2 Gridding and Interpolation

3.3 Global Energy Density

Chapter 4

3D Modeling of LEP

4.1 Overview of Previous Work

Pseudo-3D vs Scaled 2D

Geometric Factor

Chapter 5

Global and Seasonal Estimates of LEP

5.1 Overview of Previous Work

Where should you put the magnetosphere statistics? that big correlation plot of kp, ae, Dst, etc etc

Chapter 6

Satellite Instrumentation for LEP Measurement

6.1 VPM Mission Overview

6.2 Hardware Architecture

6.2.1 Wave Measurement

6.2.2 Particle Measurement

6.3 Firmware Architecture

Chapter 7

Conclusions

Appendix A

Reference Equations

A.1 Landau Damping

In raytracing, we calculate wave growth and attenuation according to Landau damping. We use the *Brinca* (1972) formulation – itself a reorganization of *Kennel* (1966) – which assumes a cold background plasma, onto which a small thermal electron population is ascribed. The following (frustratingly complex) equation set is taken from *Brinca* (1972), and reprinted here for organization.

Calculating a growth rate begins simply: we assume a time-varying plane wave in the usual complex (“phasor”) form:

$$E \sim E_0 e^{i(\omega t - \mathbf{k} \cdot \mathbf{r})} \quad (\text{A.1})$$

If either ω or \mathbf{k} have an imaginary component, then the result will be an additional real-valued term, which we can factor out as χ :

$$E = E_0 e^{i(\omega t - (\mathbf{k}_r + i\mathbf{k}_i) \cdot \mathbf{r})} \quad (\text{A.2})$$

$$= E_0 e^{-\chi r} e^{i(\omega t + \mathbf{k} \cdot \mathbf{r})} \quad (\text{A.3})$$

If the new exponential term $-\chi$ is positive, the wave will be amplified; if the term is negative, the wave will be attenuated.

The spatial growth rate χ is given by equation A.4 (*Brinca*, 1972; *Kennel*, 1966):

$$\chi = -\frac{ck_i}{\omega} = \frac{\delta}{4\eta(2A\eta^2 - B)}(T_1 - T_2 - T_3) \quad (\text{A.4})$$

with the following terms:

$$\begin{aligned} T_1 &= \frac{\eta^2 \sin^2 \theta - P}{2(S - \eta^2)} \Gamma_I \cdot [(R - \eta^2)J_{m-1} + (L - \eta^2)J_{m+1}]^2 G_1 \\ T_2 &= 2[(S - \eta^2 \cos^2 \theta)(S - \eta^2) - D^2] \Lambda_I J_m G_2 \\ T_3 &= 2\eta^2 \sin \theta \cos \theta \Gamma_I \cdot [(R - \eta^2)J_{m-1} + (L - \eta^2)J_{m+1}] G_2 \end{aligned} \quad (\text{A.5})$$

where $\chi > 0$ indicates damping.

Note that *Brinca* has related the temporal damping rate ω_i from *Kennel* (1966) to a spatial damping rate k_i by assuming a constant propagation at the group velocity v_g .

A, B, C, D, L, P, R , and S are the Stix environment parameters given by 2.26 – 2.27, and are functions of wave frequency, local plasma density, and local magnetic field strength.

As previous, θ is the angle between the wavenormal vector and the background magnetic field, and η is the wave refractive index, found by solving equation 2.30.

The terms J_m, J_{m+1} and J_{m-1} are Bessel functions of the first kind, which account for the multiple resonant modes – $m = 0$ indicates the Landau resonance; $m \pm 1$ the Cyclotron resonance.

The terms Γ_I and Λ_I are summations over resonant modes $m \in \{-\infty \dots \infty\}$, and integrations over the velocity space v_\perp, v_\parallel given by:

$$\Gamma_I = \frac{2\pi^2\omega_p^2}{\omega k_{\parallel}} \sum_{m=-\infty}^{\infty} \int_0^{\infty} v_{\perp}^2 dv_{\perp} \int_{-\infty}^{\infty} \delta(v_{\parallel} - V_m) dv_{\parallel} \quad (\text{A.6})$$

$$\Lambda_I = \frac{2\pi^2\omega_p^2}{\omega k_{\parallel}} \sum_{m=-\infty}^{\infty} \int_0^{\infty} v_{\perp} dv_{\perp} \int_{-\infty}^{\infty} v_{\parallel} \delta(v_{\parallel} - V_m) dv_{\parallel} \quad (\text{A.7})$$

$$V_m = \frac{\omega - m\omega_c}{k_{\parallel}} \quad (\text{A.8})$$

Finally, the temperature distribution is included in the values G_1 and G_2 – each of which are functions of the *gradient* of the phase-space distribution function:

$$f = f(\mathbf{x}, \mathbf{v}) = f(\mathbf{x}, v_{\perp}, v_{\parallel}):$$

$$G_1 = \left(1 - \frac{k_{\parallel} v_{\perp}}{\omega}\right) \frac{\partial f}{\partial v_{\perp}} + \frac{k_{\parallel} v_{\perp}}{\omega} \frac{\partial f}{\partial v_{\parallel}} \quad (\text{A.9})$$

$$G_2 = J_m \left[\left(1 + \frac{m\omega_c}{\omega}\right) \frac{\partial f}{\partial v_{\parallel}} - m \frac{\omega_c}{\omega v_{\perp}} \frac{\partial f}{\partial v_{\perp}} \right] \quad (\text{A.10})$$

Despite the complexity of these equations, the phase-space distribution function f is the only fundamental new input – every remaining parameter is an output of the raytracer, and itself a result of our plasma density and magnetic field models.

Our implementation, derived from *Golden et al.* (2010), computes the gradients of f numerically using finite differencing, therefore granting the flexibility to use any arbitrary distribution function.

Appendix B

Runge-Kutta Methods

Bibliography

- Angerami, J. J. (1963), Studies of Planetary Atmospheres 1., *Distribution*, 69(21).
- Appleton, E. V. (1932), Appleton : Wireless Studies of the Ionosphere . Wireless Studies of the Ionosphere .* Appleton : Wireless Studies of the Ionosphere ., (10).
- Bell, T. F. (1984), The nonlinear gyroresonance interaction between energetic electrons and coherent VLF waves propagating at an arbitrary angle with respect to the Earth's magnetic field, *Journal of Geophysical Research*, 89(A2), 905–918, doi:10.1029/JA089iA02p00905.
- Bell, T. F. (2002), The Landau damping of magnetospherically reflected whistlers within the plasmasphere, *Geophysical Research Letters*, 29(15), 2–5, doi:10.1029/2002GL014752.
- Bilitza, D., and B. W. Reinisch (2008), International Reference Ionosphere 2007: Improvements and new parameters, *Advances in Space Research*, 42(4), 599–609, doi:10.1016/j.asr.2007.07.048.
- Bittencourt, J. A. (2004), *Fundamentals of Plasma Physics*, 3rd ed.
- Blaes, P. R., R. A. Marshall, and U. S. Inan (2016), Global occurrence rate of elves and ionospheric heating due to cloud-to-ground lightning, *Journal of Geophysical Research A: Space Physics*, 121(1), 699–712, doi:10.1002/2015JA021916.
- Bortnik, J. (2005), Precipitation of radiation belt electrons by lightning-generated magnetospherically reflecting whistlers, Ph.D. thesis, Stanford University.

- Bortnik, J., U. S. Inan, and T. F. Bell (2006), Temporal signatures of radiation belt electron precipitation induced by lightning-generated MR whistler waves: 1. Methodology, *Journal of Geophysical Research: Space Physics*, *111*(2), 1–22, doi:10.1029/2005JA011182.
- Bortnik, J., R. M. Thorne, and N. P. Meredith (2007), Modeling the propagation characteristics of chorus using CRRES suprathermal electron fluxes, *Journal of Geophysical Research: Space Physics*, *112*(8), 1–13, doi:10.1029/2006JA012237.
- B.Peter, W. (2007), Quantitative Measurement of Lightning-Induced Electron Precipitation Using Vlf Remote Sensing, (February).
- Brinca, A. L. (1972), On the Stability of Obliquely Propagating Whistlers, *Journal of Geophysical Research*, *77*(19), 3495–3507.
- Bruce, C. E. R., and R. H. Golde (1941), The Lightning Discharge, *The Journal of the I.E.E.E.*, *88*(6), 487–505.
- Carpenter, D. L., and R. R. Anderson (1992), An ISEE / Whistler Model of Equatorial Electron Density in the Magneto sphere Od D ' j ;, *J. Geophys. Res.*, *97*, 1097–1108.
- Cayton, T. E. (2005), Phase-Space Density Analyses of the AE-8 Trapped Electron and the AP-8 Trapped Proton Model Environments, *Tech. rep.*, Office of Scientific and Technical Information, Oak Ridge, TN, Los Alamos, NM.
- Chandler, O., M. O. Chandler, J. H. Waite, and T. E. Moore (1991), Observations of polar ion outflows, *Journal of Geophysical Research: Space Physics*, *96*(A2), 1421–1428, doi:10.1029/90JA02180.
- Chang, H. C., and U. S. Inan (1983), Quasi-relativistic electron precipitation due to interactions with coherent VLF waves in the magnetosphere, *Journal of Geophysical Research*, *88*(A1), 318–328.
- Chen, F. F. (1983), *Introduction to Plasma Physics and Controlled Fusion*, Plenum PRes, New York, NY, doi:QC718.C39 1983.

- Cohen, M. B., N. G. Lehtinen, and U. S. Inan (2012), Models of ionospheric VLF absorption of powerful ground based transmitters, *Geophysical Research Letters*, *39*(24), 1–5, doi:10.1029/2012GL054437.
- Cotts, B. R. T. (2011), Global Quantification of Lightning-Induced Electron Precipitation Using Very Low Frequency Remote Sensing, Ph.D. thesis.
- Edgar, B. (1972), The structure of the magnetosphere as deduced from magnetospherically reflected whistlers, Ph.D. thesis, Stanford University.
- Fehlberg, E. (1969), Low-order classical Runge-Kutta formulas with stepsize control and their application to some heat transfer problems, *Tech. Rep. July*, NASA.
- Gallagher, D. L., P. D. Craven, R. H. Comfort, and T. E. Moore (1995), On the azimuthal variation of core plasma in the equatorial magnetosphere, *Journal of Geophysical Research: Space Physics*, *100*(A12), 23,597–23,605, doi:10.1029/95JA02100.
- Gallagher, D. L., P. D. Craven, and R. H. Comfort (1999), Global Core Plasma Model, *Journal of Geophysical Research: Space Physics*, *105*(A8), 18,819–18,833, doi:10.1029/1999JA000241.
- Golden, D. I., M. Spasojevic, F. R. Foust, N. G. Lehtinen, N. P. Meredith, and U. S. Inan (2010), Role of the plasmopause in dictating the ground accessibility of ELF/VLF chorus, *Journal of Geophysical Research: Space Physics*, *115*(11), 1–15, doi:10.1029/2010JA015955.
- Graf, K. L., N. G. Lehtinen, M. Spasojevic, M. B. Cohen, R. A. Marshall, and U. S. Inan (2013), Analysis of experimentally validated trans-ionospheric attenuation estimates of VLF signals, *Journal of Geophysical Research: Space Physics*, *118*(5), 2708–2720, doi:10.1002/jgra.50228.
- Griffiths, D. J. (1999), *Introduction to Electrodynamics*, 3rd ed., Prentice-Hall, Inc, Upper Saddle River, New Jersey.

- Haselgrove, J. (1954), Ray theory and a new method for ray tracing, *Report of the Physical Society Conference on Physics of the Ionosphere*, pp. 355–364.
- Haselgrove, J., and C. B. Haselgrove (1960), Twisted ray paths in the ionosphere, *Proceedings of the Physical Society*, 75, 357–363, doi:10.1088/0370-1301/70/7/302.
- Helliwell, R. A. (1965), *Whistlers and Related Ionospheric Phenomena*, Stanford University Press.
- Heney, F. S. (1980), Improved ray description of wave equations, *Physical Review Letters*, 45(24), 1897–1900, doi:10.1103/PhysRevLett.45.1897.
- Jasna, R.-D. L. (1993), Gyroresonant Scattering of Radiation Belt Electrons by Oblique Whistler Waves, Ph.D. thesis, Stanford University.
- Kennel, C. (1966), Low-Frequency Whistler Mode, *Physics of Fluids*, 9(11), 2190, doi:10.1063/1.1761588.
- Kimura, I. (1966), Effects of Ions on Whistler-Mode Ray Tracing, *Radio Science*, 1(3), 269–283, doi:10.1002/rds196613269.
- Kulkarni, P. (2009), Controlled precipitation of radiation belt electrons, Ph.D. thesis, Stanford University, doi:10.1029/2002JA009580.
- Landau, L. D. (1946), On the vibrations of the electronic plasma, *Soviet Journal of Physics*.
- Lauben, D. (1998), Precipitation of radiation belt Electrons by obliquely-propagating lightning-generated whistler waves, Ph.D. thesis, Stanford University.
- Marshall, R. A., J. Bortnik, N. Lehtinen, and S. Chakrabarti (2011), Optical signatures of lightning-induced electron precipitation, *Journal of Geophysical Research: Space Physics*, 116(8), 1–8, doi:10.1029/2011JA016728.
- Mathews, J. H., and K. D. Fink (2004), *Numerical Methods Using Matlab*.

- McIlwain, C. E. (1961), Coordinates for mapping the distribution of magnetically trapped particles, *Journal of Geophysical Research*, *66*(11), 3681–3691, doi:10.1029/JZ066i011p03681.
- Ngo, H. D. (1989), Electrostatic waves stimulated by VLF whistler mode waves scattering from magnetic-field-aligned plasma density irregularities, Ph.D. thesis, Stanford University.
- Persoon, A. M., D. A. Gurnett, and S. D. Shawhan (1983), Polar cap electron densities from DE 1 plasma wave observations, *Journal of Geophysical Research: Space Physics*, *88*(A12), 10,123–10,136, doi:10.1029/JA088iA12p10123.
- Sazhin, S. (1993), *Whistler-mode Waves in a Hot Plasma*, 1 ed., Cambridge University Press, Cambridge.
- Starks, M. J., R. A. Quinn, G. P. Ginet, J. M. Albert, G. S. Sales, B. W. Reinisch, and P. Song (2008), Illumination of the plasmasphere by terrestrial very low frequency transmitters: Model validation, *Journal of Geophysical Research: Space Physics*, *113*(9), 1–16, doi:10.1029/2008JA013112.
- Stix, T. H. (1992), *Waves in Plasmas*, American Institute of Physics, New York, NY, doi:QC718.5.W3S75.
- Thébault, E., C. C. Finlay, C. D. Beggan, P. Alken, J. Aubert, O. Barrois, F. Bertrand, T. Bondar, A. Boness, L. Brocco, E. Canet, A. Chambodut, A. Chuliat, P. Coïsson, F. Civet, A. Du, A. Fournier, I. Fratter, N. Gillet, B. Hamilton, M. Hamoudi, G. Hulot, T. Jager, M. Korte, W. Kuang, X. Lalanne, B. Langlais, J.-M. L  ger, V. Lesur, F. J. Lowes, S. Macmillan, M. Manda, C. Manoj, S. Maus, N. Olsen, V. Petrov, V. Ridley, M. Rother, T. J. Sabaka, D. Saturnino, R. Schachtschneider, O. Sirol, A. Tangborn, A. Thomson, L. T  ffner-Clausen, P. Vigneron, I. Wardinski, and T. Zvereva (2015), International Geomagnetic Reference Field: the 12th generation, *Earth, Planets and Space*, *67*(1), 79, doi:10.1186/s40623-015-0228-9.

- Tsyganenko, N. A., and M. I. Sitnov (2005), Modeling the dynamics of the inner magnetosphere during strong geomagnetic storms, *Journal of Geophysical Research: Space Physics*, *110*(A3), 1–16, doi:10.1029/2004JA010798.
- Vette, I. (1991), The Model Trapped Electron Environment, *Environment*.
- Vette, J. I. (1966), Models of the Trapped Radiation environment: Volume I: Inner Zone Protons and Electrons, *Tech. rep.*, Scientific and Technical Information Division; National Aeronautics and Space Administration (NASA).